Composites Part C: Open Access 15 (2024) 100542

Contents lists available at ScienceDirect

Composites Part C: Open Access

journal homepage: www.sciencedirect.com/journal/composites-part-c-open-access

Damage detection in composite and plastic thin-wall beams by operational modal analysis: An experimental assessment

Josué Pacheco-Chérrez [a], Manuel Aenlle [b], Pelayo Fernández [b], Carlos Colchero [a], Oliver Probst [a,*]

[a] Tecnologico de Monterrey, School of Engineering and Sciences, Eugenio Garza Sada 2051, Monterrey 64849, Mexico
[b] Department of Construction and Manufacturing Engineering, University of Oviedo, Gijón 33204, Spain

ARTICLE INFO

Keywords:
Thin-wall beam
Composites
Plastics
Operational modal analysis
Experiment

ABSTRACT

The detection and localization of different damage features in thin-wall beam composite and plastic beams using Operational Modal Analysis (OMA) has been demonstrated experimentally. The detection of small damage features using modal analysis techniques is an emerging field, with few experimental OMA-based assessments having been reported so far. The proposed method is based on OMA combined with Stochastic Subspace Identification (SSI) and the enhancement of damage features by Continuous Wavelet Transforms (CWT). A composite thin-wall beam (CTWB) structure in two measurement configurations and a PVC tube in a free-free configuration have been tested. Damage features detected include extra masses attached to the beam, with a range from 9.5 % to 14.0 % of the beam mass, and small cracks perpendicular to the beam axis with lengths of about 4 % of the perimeter of the cross section. Calibration curves relating the strength of the damage signal with the weight of the attached masses have been constructed. Two simultaneous cracks or two masses could be detected as well. The quantification and localization of damage feature along the beam was possible through the use of Gaussian fit surface applied to damage maps obtained with the CWT technique. The width of the Gaussian fit curve was of the order of the distance between accelerometers, but the accuracy, estimated to be around 3 % of the beam length, was found to have sub-grid resolution. The proposed method was shown to work reliably with a relatively coarse measurement grid, potentially allowing for cost-effective Structural Health Monitoring (SHM) approaches.

1. Introduction

Structural health monitoring is an important tool to guarantee the integrity of a structure and detect damage features in early stages in order to avoid structural failure and environmental hazards. Methods based on the dynamic characteristics of structures have become attractive in different fields like civil, mechanical, and aerospace engineering due to their ease of implementation. Vibration-based damage detection is based on the fact that damage alters the dynamic characteristics, i.e., the modal parameters of the structure, such as its natural frequencies, its modal damping values, and its mode shapes. The reconstruction of the modal parameters allows for a full determination of the structure's dynamic behavior. Two of the widely used techniques in modal analysis are Experimental Modal Analysis (EMA) and Operational Modal Analysis (OMA). EMA is generally performed in a controlled laboratory environment where the force applied to the structure is measured along with the response signals. OMA, on the other hand, is typically performed under real-life conditions and relies only on signals retrieved from the structure, with the exciting forces being unknown [1].

Different authors have used EMA for the extraction of modal parameters and subsequent damage detection in different types of structures. Brethee et al. [2] presented an improved curvature damage factor (ICDF) analysis for damage detection in Carbon Fiber Reinforced Polymer (CFRP) laminated plates in a work where a 3D robotic scanning laser vibrometer (SLV) was used to take 65 measurements in a line to obtain the experimental modal parameters. The authors detected a 20 mm x 1 mm fiber break [2]. Dahak et al. used experimental modal analysis and 18 equidistant measurement points on a cantilever beam for the detection of 20.4 × 4.2 mm saw cuts through changes in measured frequency and curvature mode shapes [3]. Dolinski et al. used an SLV to take measurement data of 200 points to obtain modal parameters of a wind turbine rotor blade and then used one-dimensional wavelet analysis for damage detection [4]. A steel element was fixed to the structure to simulate damage in the wind turbine blade [4].

---

* Corresponding author.
E-mail address: oprobst@tec.mx (O. Probst).

https://doi.org/10.1016/j.jcomc.2024.100542

Abdulkareem et al. used a two-dimensional continuous wavelet transform (2D-CWT) to detect damage in steel plate structures; in the experimental part, 25 response accelerations were taken to detect a damage feature of 40 mm x 40 mm x 0.8 mm. Pacheco-Chérrez et al. used 12 sequential acceleration measurements to obtain modal parameters in an aluminum cantilever beam. The authors demonstrated a reliable approach to damage detection through a combination of wavelet analysis, image similarity metrics (ISM) applied to full wavelet scalograms, and a digital twin approach to solving the missing baseline problem, combined with an ensemble method to account for materials properties uncertainties. ANN methods were used as a reference, but were shown to be inferior to the image similarity approach [5]. Pacheco-Chérrez et al. [6] demonstrated the detection, localization, and quantification of cracks in composite thin-walled beams with a length of 550 mm using experimental modal analysis based on a 3 × 50 measurement grid scanned manually with a laser vibrometer. Crack lengths down to 2 mesh cells were readily detected; the simultaneous detection of two cracks was also demonstrated. The efficiency of the method in terms of its sampling requirement was shown to be higher than in most published works. Chinka et al. applied experimental modal testing (EMT) to damage detection by curvatures and natural frequencies in an aluminum cantilever beam with eight acceleration measurements [7]. The authors analyze 25 mm crack type damage features with a depth varying between 1 mm and 5.83 mm [7].

Operating Modal Analysis (OMA), on the other hand, is a well-established method for analyzing large-scale engineering structures such as wind turbines [8,9], bridges [10], and towers; however, its application to small damage features such as cracks and holes is still incipient. Xu et al. proposed a method which combines Ramanujan Subspace Projection (RSP) and Covariance-Driven Stochastic Subspace Identification (Cov-SSI) to extract the modal parameters in wind turbines under harmonic excitation [11]. The authors did, however, not analyze any damage. In another work, Xu et al. used flexural Operating Deflection Shapes (ODS) with 255 velocity responses acquired by a 3D SLV in an aluminum plate for structural damage detection. The method detected and located a notch of 20 mm × 20 mm [12]. Altunisik et al. used Enhanced Frequency Domain Decomposition (EFDD) and SSI for OMA to obtain modal parameters in steel cantilever beams [13]. The authors used a combination of six measurements of accelerometers and an inverse problem (IP) formulation with a sampling number of 102 for damage detection in a beam with multiple cracks. Di Lorenzo et al. used both EMA and OMA to obtain modal parameters in two blades in free-free boundary conditions and cantilever conditions. 120 measurement points were defined to cover the entire surface of the blade with a length of 14.3 m. No attempt was made to detect damage [14]. Xu et al. used OMA with 200 virtual measurement points measured with a Continuously Scanning Laser Doppler Vibrometer (CSLDV), where the curvature damage index was used to detect damage in a cantilever beam [15]. Pacheco & Probst [16] presented a Finite Element Analysis (FEA) of an aluminum cantilever beam with multiple cracks under white noise excitation. The authors used nine acceleration signals and demonstrated the use of OMA for damage detection. Rinaldi et al. [17] used Frequency Domain Decomposition (FDD) and SSI to obtain the modal parameters of a small-scale frame structure. In this work, the authors used two measurement systems, one based on a fast camera and another on an array of 24 accelerometers [17]. The authors conducted a comparison between the results of both schemes and found similar results, with both methods found to be capable of detecting the damage feature [17]. Migot and Giurgiutiu analyzed delamination in composite plates. The experiments included electromechanical impedance spectroscopy (EMIS) and SLDV; the area analyzed was 110 mm x 110 mm, and the SDLV scanned the area with a 1 mm of resolution [18]. Migot et al. investigated fatigue crack detection in composite plates with a combination of a piezoelectric wafer active sensor (PWAS) and an SLDV. The size of the area analyzed was 45 mm x 90 mm, with a crack length of 18 mm; the element size of the grid was 2 mm [19].

A summary of the experimental work on damage detection with modal techniques has been compiled in Table 1, allowing for a comparison of relevant experimental aspects such as sample size, fault size, and number of sensors or measurement positions used. The authors of [3,5,7] used accelerometers with 8, 18, and 12 measurement points in an EMA setting to obtain modal parameters in a simple structure like cantilever beams. In other works [2,20], EMA has been applied to damage detection in simple plates, where a 3D-SLV with 65 measurement points was used in [2], whereas accelerometers at 25 measurement locations were employed in [20]. In subsequent work, EMA was used to obtain modal parameters in more complex structures like WT blades with 200 measurement points [4] and composite TWB with 150 measurement points [6]. While all previous work was based on EMA, a few groups of authors have used OMA for damage detection. In Ref. [21], CLSDV with 200 measurement points was applied to damage detection in aluminum beams. The authors of [18,19,22] use OMA for damage detection in plates with 990, 12,100, and 1521 measurement points. In reference [17], a combination between a fast camera and accelerometers with 24 measurement points was employed for damage detection in 4-story shear-type steel. Of all the works discussed above, most of them analyze simple structures such as beams and plates. And in both works on more complex structures such as blades and TWB, it was necessary to have a large number of measurement points (150 and 200) along the structure.

From the discussion in the preceding paragraph, several important conclusions can be drawn: (1) Operational Modal Analysis (OMA), despite being a relatively established technique in other fields of study such as civil engineering, is still an incipient technique for the detection of small damage features in beams and plates. (2) Most published work focuses on proofs-of-concept and certain methodological improvements. (3) The high-accuracy detection of damage features is mostly limited to laser scanning techniques with a high-resolution measurement grid. (4) Quantification of damage is seldom reported. (5) Samples investigated are mostly simple beams and plates; damage in thin-walled beam structures made from composite material (CTWB) has not been analyzed. (6) A systematic analysis of damage in CTWB structure for different damage features, different damage intensity, and measurement configuration has not been reported yet.

The present work has been designed to fill some of these voids. In the following, we will report on the detection of damage in two different sample types, a CTWB structure and a PVC tube, and several boundary conditions. The CTWB structure was analyzed both in a cantilevered and a suspended configuration, whereas the PVC tube was measured in an arrangement with two free ends. Seven pairs of accelerometers were placed at fixed positions along the beam axis in all cases. Different types of damage features were analyzed, including attached additional weights (in the case of the CTWB structure) and cuts perpendicular to the beam axis (for both the CTWB and PVC samples). It will be shown that (a) all damage features can be detected and located with sub-grid accuracy, (b) damage intensity can be quantified, and (c) pairs of damage features can be accurately detected. The rest of the manuscript is organized as follows. Section 2 presents an overview of the methodology used in this work and the theoretical framework of the Stochastic Subspace Identification (SSI) method and the Continuous Wavelet Transform (CWT) used in this work. Section 3 provides a detailed account of the algorithm implemented, including the concept of predominant mode shapes, the turnover transformation and the interpolation of mode shapes, the damage metric, and the surface fitting approach used for the precise location of the damage feature and the quantification of the damage intensity. Section 4 describes the experimental setup, and the damage cases analyzed. In Section 5 the results of all experiments are shown and discussed. Section 6 provides a summary and the conclusions of this work, including its limitations and the suggested areas of future research.

Table 1
Recent work on damage detection with modal analysis. Abbreviations used in this table: (a) Methods: ICDF Improved Curvature Damage Factor; HFMA High Frequency Modal Analysis; MRIV Mode Ranking Index Value; COMAC = Coordinate Modal Assurance Criterion; EMA = Experimental Modal Analysis; OMA = Operational Modal Analysis; MA = Modal Analysis. (b) Measurement equipment: SLV = Scanning Laser Vibrometer, LSV = Laser Scanning Vibrometry; CSLDV = Continuously Scanning Laser Doppler Vibrometer; EMIS = Electromechanical Impedance Spectroscopy; SLDV = Scanning Laser Doppler Vibrometer; PWAS = Piezoelectric Wafer Active Sensor.

Refs.	Structure	Structure dimensions	Fault size	Meas. Equipment	Meas. points	Method	MA techn.
[2]	CFRP laminated plates	200 × 100 × 125	200 × 1 mm^2	3D robotic SLV	65	ICDF	EMA
[3]	Cantilever beam	380 × 20.4 × 7.6	saw cut 20.4 × 4.2	Accelerometers	18	CMS	EMA
[4]	WTB	1740 mm length	Surface-attached steel element	LSV	200	1D-WA	EMA
[20]	Steel plate	560 × 560 × 3.2	80 × 80 mm^2	Accelerometers	25	MSD 2D-CWT	EMA
[5]	Aluminum cantilever beam	840 × 38.1 × 4.8	38.1 × 10 × 2	Accelerometers	12	WA & IMS	EMA
[6]	Composite TWB	Major axis: 100 mm, minor axis: 60 mm, length = 585 mm	40, 60, 80 mm	Laser vibrometer	150	MSD & CMS	EMA
[7]	Aluminum cantilever beam	800 × 25 × 10	25 x (1 to 5.83) mm^2	Accelerometers	8	CMS & freqs.	EMA
[15]	Aluminum beams	875 × 12.7 × 5	12.7 × 12.7 × 1.825 mm^3	CLSDV	200	CDI	OMA
[22]	Aluminum plate	380 × 380 × 3	Notch 20 × 20 mm^2	3D SLV	1521	ODS	OMA
[17]	4-story shear-type steel structure	Height: 800 mm, L shaped: 50 × 50 × 4 mm^3	Removal of steel bracing	Accelerometers & fast camera	24	COMAC & DI	OMA
[18]	Composite plates	Area analyzed: 110 × 110 mm^2	Ø25 Ø50 Ø75	EMIS and SDLV	110 × 110	HFMA	OMA
[19]	Composite plates	Area analyzed: 45 × 90 mm^2	18	EMIS/PWAS and SLDV	22 × 45	MRIV	OMA

2. Methodology overview

An overview of the methodology used in this work is presented in the flow diagram of Fig. 1. The process starts with the acquisition of the output time series of the vibrating test structure; seven pairs of accelerometers were used to probe each of the samples. These output time series were then processed using the SVD (Singular Value Decomposition)/SSI (Stochastic Subspace Identification) technique, which produces the mode shapes of the structure. An interpolation step using splines was carried out next, making up for the low number of accelerometers used. An extension of the modal shapes was then applied to avoid boundary problems which could mask the failure when using the Continuous Wave Transforms (CWT). The extended and interpolated mode shapes were then fed into the CW transform, allowing the damage metric to be calculated. Using the scale factor s of the CWT as a free parameter, damage maps were then created in (v, s)-space, where v is the coordinate along the beam axis of the sample. After discriminating the damage signal from background noise, a bivariate Gaussian surface was fitted to the damage signal, allowing for a precise localization and quantification of the damage feature.

2.1. Operational modal analysis

In this work, the Stochastic Subspace Identification (SSI) method, as implemented in the software suite ARTeMIS [23], was used for OMA. In the following, a summary of the procedure will be provided for completeness. The narrative is based on the descriptions provided by Anderson [24], Brincker & Anderson [25], and Peeters & de Roeck [26].

In the SSI technique, a parametric model is fitted directly to the output time series data, by minimizing the deviation between the predicted response of the model system and the measured system response. The dynamic behavior of an n degree-of-freedom (DOF) system is governed by [25,26]

$$M\ \ddot{U}(t) + C\ \dot{U}(t) + K\ U(t) = F(t) \tag{1}$$

where$M,\ C,\ K \in \mathrm{R}^{n \times n}$are the mass, damping, and stiffness matrices, respectively, and $F(t) \in \mathrm{R}^{n \times 1}$ and $U(t) \in \mathrm{R}^{n \times 1}$ are the excitation force and the displacement vector at continuous time t, respectively. Eq. (1) can be transformed into the state equation [26]

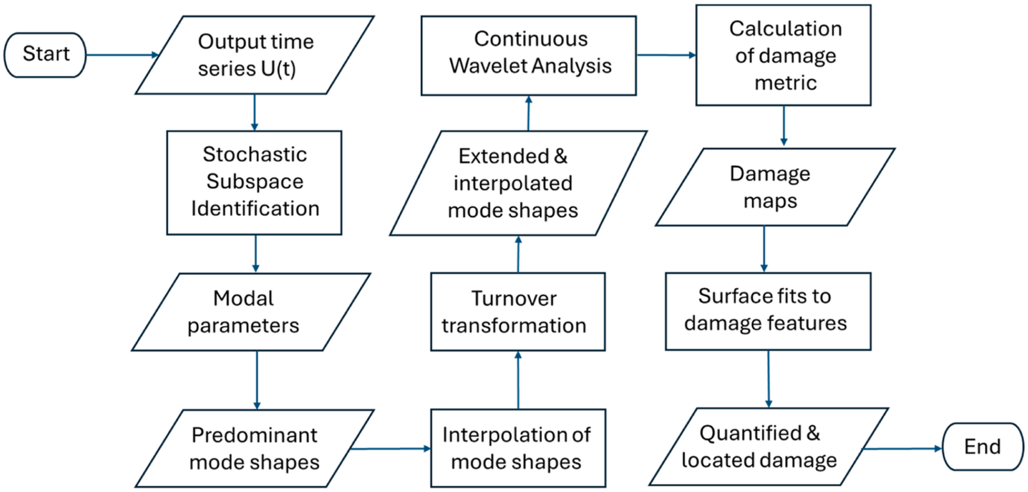

Fig. 1. Overview of the methodology used in this work.

$$\begin{aligned} \dot{x}(t) &= A_c x(t) + B_c u(t) + \widetilde{w}(t) \\ y(t) &= Cx(t) + Du(t) + \widetilde{v}(t), \end{aligned} \tag{2}$$

where $x = [U(t)\ \dot{U}(t)]^T$ is the state vector and y is the observation vector, collecting information from acceleration, velocity, and displacement sensors at certain positions. u is the external input. The matrix C collects information about the measurement process (known prior to the analysis) and the system properties (to be determined). $\widetilde{w}$ and $\widetilde{v}$ are noise vectors with a Gaussian distribution. In the SSI formalism it is generally assumed that the state vector x is not measured and has to be estimated from the observed values of y.

In the case of operational modal analysis, the input u is not known; therefore, the terms $B_c u(t)$ and $Du(t)$ can be grouped together with their respective noise terms. Also writing the resulting equation in a discrete form we obtain the following expressions:

$$\begin{aligned} x_{t+1} &= Ax_t + w_t \\ y_t &= Cx_t + v_t, \end{aligned} \tag{3}$$

where the input is now fully modelled by the noise terms w_t,v_t. Eq. (3) can be cast into the form of the Riccati equation, where the (unobserved) internal state values x_t have been replaced by predicted values $\widehat{x}_t$:

$$\begin{aligned} \widehat{x}_{t+1} &= A\widehat{x}_t + K_t e_t \\ y_t &= C\widehat{x}_t + e_t. \end{aligned} \tag{4}$$

In Eq. (4), K is the Kalman gain, and e_t is the innovation at discrete time t. Eq. (4) can be extended to a sequence of j predicted internal states and measured output values, ranging from an initial value $\widehat{x}_i$ to final value $\widehat{x}_{i+j-1}$, and correspondingly, y_i to y_{i+j-1}. The resulting equation then has the following form:

$$\begin{bmatrix} \widehat{x}_{i+1} & \widehat{x}_{i+2}\dots & \widehat{x}_{i+j} \\ y_i & y_{i+1}\dots & y_{i+j-1} \end{bmatrix} = \begin{bmatrix} A \\ C \end{bmatrix} \begin{bmatrix} \widehat{x}_i & \widehat{x}_{i+1}\dots & \widehat{x}_{i+j-1} \end{bmatrix} + \begin{bmatrix} \rho_w \\ \rho_v \end{bmatrix}, \tag{5}$$

with certain expressions ρ_w and ρ_v for the noise terms. From Eq. (5), the matrices A and C can be obtained from the regression problem

$$\begin{bmatrix} A \\ C \end{bmatrix} = \begin{bmatrix} \widehat{X}_{i+1} \\ Y_i \end{bmatrix} \widehat{X}_i^{-1} \tag{6}$$

where $Y_i = [y_i y_{i+1} \dots y_{i+j-1}]$, $\widehat{X}_{i+1} = [\widehat{x}_{i+1}\ \widehat{x}_{i+2}\dots\ \widehat{x}_{i+j}]$, $\widehat{X}_i = [\widehat{x}_i\ \widehat{x}_{i+1}\dots\ \widehat{x}_{i+j-1}]$, and $\widehat{X}_i^{-1}$ is the pseudo-inverse of matrix $\widehat{X}_i$. Evidently, an expression is needed for the predicted internal state sequences grouped in matrices $\widehat{X}_i$ and $\widehat{X}_{i+1}$. This is done in two steps.

Firstly, it can be shown [24,26] that the matrix of predicted future output states

$$O_i = [o_i, o_{i+1}, \dots, o_{i+j+1}], \text{ with } o_i = [\widehat{y}_i, \widehat{y}_{i+1}, \dots, \widehat{y}_{2i-1}] \tag{7}$$

can be expressed in terms of the measured outputs

$$Y_p = \left[y_0^{i-1}, y_1^{i}, \dots, y_{j-1}^{i+j-2}\right], \text{ with } y_0^{i-1} = [y_0, y_1, \dots, y_{i-1}] \tag{8}$$

i.e.,

$$O_i = L_i L_0^{-1} Y_p, \tag{9}$$

where the L matrices group covariance values at different time lags of the measured output signal y. Secondly, it can be shown that the predicted internal state values can be related to the predicted output values $\widehat{X}_i$ by means of the so-called observability matrix Γ_i:

$$\widehat{X}_i = \Gamma_i^{-1} O_i, \tag{10}$$

where Γ_i^{-1} is again a pseudo-inverse. If Γ_i^{-1} were known, the right-hand side of equation would be known and the matrices A and C containing the system parameters could be calculated. Calculating Γ_i is the final part of the SSI process. Different options are available, with the general theme being the Singular Value Decomposition (SVD) of the matrix of predicted future outputs O_i, pre- and post-multiplied by user-defined weighting matrices W_1 and W_2 [24,26]:

$$W_1 O_i W_2 = [U_1, U_2] \begin{bmatrix} S_1 & 0 \\ 0 & 0 \end{bmatrix} \begin{bmatrix} V_1^T \\ V_2^T \end{bmatrix} = U_1 S_1 V_1^T = W_1 \Gamma_\mathrm{i} \widehat{X}_i W_2 \tag{11}$$

In the case of the unweighted principal component algorithm used in this work, both matrices are taken to be equal to the unity matrix. From the two last equations of Eq. (11) we can identify Γ_i as [24,26]:

$$\Gamma_\mathrm{i} = U_1 S_1^{1/2} T, \tag{12}$$

where the non-singular matrix T represents an arbitrary similarity transform. With Γ_i having been determined the predicted internal states can be calculated and Eq. (6) can be used to calculate the system matrices A and C. To obtain the mode shapes required in this work, first an eigenvalue decomposition of A is carried out:

$$A = \Psi \Lambda \Psi^{-1} \tag{13}$$

where $\Lambda = \mathrm{diag}(\lambda_\mathrm{q})$ is a diagonal matrix with the complex eigenvalues of A and Ψ contains the eigenvectors as columns. The mode shapes at sensor locations are the observed parts and can be obtained using the equation:

$$\phi = C\Psi \tag{14}$$

The system of equations (4) can also be represented in the frequency domain by its transfer function $H(z)$:

$$H(z) = C(Iz - A)^{-1} K + I \tag{15}$$

where z is the complex variable used in the z-transform. Using the representations of Eqs. (13) and (14), the modal transfer function is expressed as:

$$H(z) = \phi(Iz - \Lambda)^{-1} \Psi + I \tag{16}$$

2.2. Continuous wavelet transform

The Continuous Wavelet Transform (CWT) was used in this work to boost the damage signals detected by suitable metrics; see Section 3.5 for its specific applications. Below we will provide a brief introduction for completeness. We start by defining a continuous mother wavelet as an oscillatory function with zero mean, i.e.,

$$\int_{-\infty}^{\infty} \psi(x)\, \mathrm{d}x = 0 \tag{17}$$

and satisfying the admissibility condition

$$\int_{-\infty}^{\infty} \frac{|\widehat{\psi}(\omega)|^2}{\omega} \mathrm{d}\omega < \infty, \tag{18}$$

where $\widehat{\psi}(\omega)$ is the Fourier transform of $\psi(x)$. A wavelet function is obtained by translating (parameter v) and scaling (parameter s) the mother wavelet, i.e.,

$$\psi_{v,s} = \frac{1}{\sqrt{s}} \psi\left(\frac{x - v}{s}\right). \tag{19}$$

With these definitions, the Continuous Wavelet Transform of a one-dimensional signal $f(x)$ can be written as

$$\mathrm{CWT}_f(v, s) = \frac{1}{\sqrt{s}} \int_{-\infty}^{\infty} f(x) \psi\left(\frac{x - v}{s}\right) \mathrm{d}x \tag{20}$$

In this work, the CWT was used to calculate the damage metric m_1;

see Section 3.5. In the case of the composite thin-wall beam (CTWB) structure, the one-dimensional CWT was applied to the differences of the predominant components $\phi^{(j)}_{\text{predom}}$ (see Section 3.2) of the mode shapes of the damaged (d) and undamaged (u) structure (i.e., $f(x) = \phi^{(j,d)}_{\text{predom}} - \phi^{(j,u)}_{\text{predom}}$), prior interpolation and extension through the turnover transformation (Section 3.4) and. In the case of the PVC tube, no such data reduction was necessary, since only one linear array of sensors was used, and the one linear set of modal data ($f(x) = \phi^{(d)}(x) - \phi^{(u)}(x)$) was used directly to calculate the damage metric.

3. The algorithm for damage detection

In the following, the main steps in the damage detection algorithm implemented in this work will be described briefly.

3.1. Modal analysis

The first step of this methodology is to obtain the natural frequencies and mode shapes of the structure. In the present work, this information was obtained using Operational Modal Analysis (OMA) based on Stochastic Subspace Identification (SSI) as described in Section 2.1. As shown in Figs. 3 and 4 for the case of the first test structure used in this work, a thin-walled beam (TWB) made from composite material in the form a hollow cylinder with elliptical cross section, the three-dimensional mode structure has been probed with a simple array of two rows of accelerometers, placed on either side of the beam along the major axis of the elliptical cross section. This experimental arrangement was based on the expectation that the lower mode shapes would be predominantly deflectional or torsional in nature, allowing for a very cost-effective sensor array.

The result of this step are the mode shape functions $\phi_{\text{left}}(x)$ and $\phi_{\text{right}}(x)$ corresponding to the left and right row of accelerometers, respectively; see Fig. 3 and Fig. 4 for a photographic illustration of the placement of these sensors. In the case of the PVC tube, only one row of accelerometers was used; see Fig. 5.

3.2. Predominant components of the mode shapes – composite beam case

In the case of composite beam or CTWB, symmetrical and antisymmetric components can be constructed for each mode j by

$$\phi^{(j)}_{\text{symm}}(x_i) = \frac{1}{2}\left(\phi^{(j)}_{\text{left}}(x_i) + \phi^{(j)}_{\text{right}}(x_i)\right) \tag{21}$$

$$\phi^{(j)}_{\text{antisymm}}(x_i) = \frac{1}{2}\left(\phi^{(j)}_{\text{left}}(x_i) - \phi^{(j)}_{\text{right}}(x_i)\right) \tag{22}$$

As shown in Section 5, all six modes analyzed in the case of the CTWB structure show indeed a predominantly deflectional or torsional behavior, depending on the mode number. Predominant components can then be defined by

$$\phi^{(j)}_{\text{predom}}(x_i) = \begin{cases} \phi^{(j)}_{\text{symm}}(x_i) & \text{if } \max\left|\phi^{(j)}_{\text{symm}}(x_i)\right| \gg \max\left|\phi^{(j)}_{\text{antisymm}}(x_i)\right| \\ \phi^{(j)}_{\text{antisymm}}(x_i) & \text{if } \max\left|\phi^{(j)}_{\text{symm}}(x_i)\right| \ll \max\left|\phi^{(j)}_{\text{antisymm}}(x_i)\right| \end{cases} \tag{23}$$

3.3. Interpolation of mode shapes

Given the limitations regarding the number of sensors that can be installed in a practical experimental setting, the OMA-reconstructed predominant mode shapes were interpolated by splines to a length of $n' = 5(3n+2)$, with n again being the number of sensor positions. In this work, the SCIPY UnivariateSpline command was used to generate the interpolated modes.

3.4. Extension of mode shapes

To avoid edge effects caused by the unstable behavior of the wavelet coefficients at the ends of the analyzed mode shape an extension of the mode shapes was performed. In this work, the isomorphism method was used. This method consists of adding an additional virtual beam to the ends of the measured mode shapes, i.e., by replicating the measured data set on either side of the actual physical structure [27]. The length of the extended signal is $n' = 3n' - 4$, with n' being the number of interpolated locations. In this work, the turnover transformation was employed. This transformation consists in reflecting the measured mode shape $\phi_0(x)$ (Eq. (12)) around the y-axis at the edge locations ($x = a$ or b), where $\phi_0(x) = \phi_{\text{predom}}(x)$ for the case of the CTWB structure. The left and right extensions are given by

$$\phi_{x<a}(x) = \phi_0(2a - x) \tag{24}$$

$$\phi_{x>b}(x) = \phi_0(2b - x) \tag{25}$$

The extended signal is then given by

$$\phi(x) = [\phi_{x<a}(x);\ \phi_0(x);\ \phi_{x>b}(x)] \tag{26}$$

In Eq. (21), the mode index$j$ has been dropped for simplicity. Fig. 2 shows a signal $\phi(x)$ after the turnover transformation procedure. The curve in black shows the result of Eq. (19). Meanwhile, curve in red shows the result of Eq. (20).

3.5. Damage metric

For damage detection and quantification, first the difference of the interpolated and extended mode shapes corresponding to the undamaged and damaged structure is calculated for each mode j:

$$\chi_j = \phi^{(u)}_j(x) - \phi^{(d)}_j(x), \tag{27}$$

where the superscript u and d stand again for the mode shapes of the undamaged and damaged mode shapes, respectively. For the case of the CTWB structure, the predominant modes were used. As described in Section 4, damage features are either small linear cracks or added masses. Then, the CWT of the squared mode shape difference is calculated:

$$\text{CWT}_{\chi_j}(v, s) = \frac{1}{\sqrt{s}} \int_{-\infty}^{\infty} \chi_j(x)\psi\left(\frac{x - v}{s}\right)\text{d}x \tag{28}$$

The CW-transformed mode shape differences are then squared:

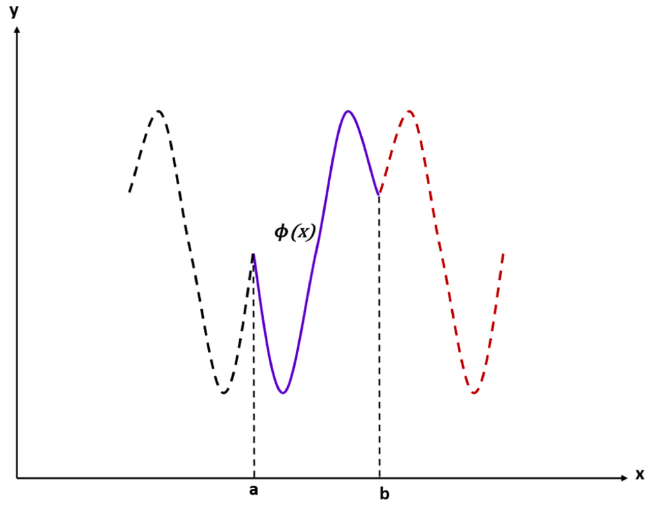

Fig. 2. Extended mode shape after the turnover transformation.

$$\mathrm{CWT}_{\chi_j^2}(v,s) = \left[\mathrm{CWT}_{\chi_j}(v,s)\right]^2 \tag{29}$$

Then, the squared CW-transformed differences for each participating mode *j* are summed and clipped to the original measurement interval [*a*, *b*] to create the metric m_1:

$$m_1(v,s) = \sum_{j=1}^{N} \mathrm{CWT}_{\chi_j^2}(v,s), \quad a \leq v \leq b \tag{30}$$

with N being the number of modes. The spatial coordinate v is now limited again to the original range of the sample, i.e., without the extensions. $m_1(v,s)$ is a function of the linear spatial coordinate v and the scale variable s and will be referred to the *scalogram* of the sample damage.

In this work, the PyWavelets command cwt was used for the CW transform, and the scales were varied between $s = 1$ and 25. The mother wavelet chosen for all the analyses was a gaus2 from the Gaussian derivatives family $f_{\mathrm{Gauss}}(x) = C_p e^{-x^2}$, with gaus2 being the second derivative of f_{Gauss}.

3.6. Damage detection and quantification

To (a) detect and (b) quantify possible damage features on the sample the following actions were taken. Firstly, a threshold value $m_{1,\mathrm{thresh}}$ was established to identify candidate regions for damage. In this work, $m_{1,\mathrm{thresh}} \sim 0.1\max(m_1)$ proved to be suitable criterion. Secondly, the sample region $\{(v, s)|a \leq v \leq b, 1 \leq s \leq 25\}$ was clipped to subregion (s) where $m_1(v,s) \geq m_{1,\mathrm{thresh}}$. Thirdly, an attempt was made to fit a bidimensional Gaussian function

$$f_{\mathrm{fit}}(v,s) = A\exp\left[a(v - v_0)^2 + b(v - v_0)(s - s_0) + c(v - v_0)^2\right] \tag{31}$$

to the signal $m_1(v,s)$ in the clipped region(s). In all cases reported in this work this procedure provided good results. While Eq. (31) allows for a rotation of the fit function in practice $|b| \ll |a|, |c|$, i.e., rotations can generally be neglected.

4. Experimental setup

The experiments were conducted with uniaxial accelerometers with a sensitivity of 100 mV/g and a 16-channel data acquisition system from TEAC, series LX-120. A sampling frequency of 5000 Hz and an acquisition time of 5 min was used in all experiments. The software package ARTeMIS from Structural Vibrations Solutions [23] was used to process the acquired information, using the Stochastic Subspace Identification (SSI) methodology described in Section 2. The test structures (further described below) were excited by manual hammer tapping, with the excitations tending to be stochastic both in time and space. Given that all experiments were conducted in OMA mode, the excitation signals were not recorded. The full experiment was repeated several times for each sample in order to allow for an assessment of consistency.

The first structure analyzed is a thin-walled beam (TWB) with a constant elliptical section made from composite material and the following dimensions: major axis = 100 mm, minor axis = 60 mm, and length 580 mm. This elliptical cylinder is hollow throughout, with an open end on one side and an end cap made of the same material at the other. The materials properties of the composite are shown in Table 2.

Table 2
Materials properties of test structure 1 (composite thin-walled beam (CTWB)).

Property	Parameters	Value	Unit
Elasticity modulus	E11	32.296	GPa
	E22=E33	13.971	GPa
Shear modulus	G12	6.987	GPa
	G13=G23	5.756	GPa
Poisson's ratio	V12	0.262	
	V13=V23	0.312	

During the first experimental setup, the elliptical cylinder was cantilevered with the non-hollow (capped) end embedded in a solid support structure. Measurements were taken with 14 accelerometers, with 7 each placed on opposing sides along the major axis of the ellipse, as shown in Fig. 3 (*left*). For the emulation of damage, different masses were placed on the upper face of the ellipse near sensor five (approximately at the axial position $v = 5.4$) as shown in Fig. 3 (*right*), with the masses being screwed to the structure using a nut and a bolt. The measurement direction of the accelerometers was normal to the main axis of the cylinder.

In the second configuration the composite beam was suspended vertically from the laboratory ceiling as shown in Fig. 4 (*left*), with the suspension fixture being screwed to the end cap of the otherwise hollow beam. In the same arrangement as in the cantilever configuration, a total of 14 accelerometers were used, with 7 sensors placed at each side of the structure, measuring in the direction normal to the axis of the structure. Masses of different weights were screwed onto the central part of the upper face of the ellipse between sensors 5 and 6 (see Fig. 4 (*right*)) as before.

In the third configuration a second test structure, a UNE-EN 1329 13,501 PVC tube with $E = 3.2$ GPa, diameter 110 mm, and length 2000 mm was used. 7 accelerometers were placed in the central part of the upper face and 7 on one side of the tube as shown in Fig. 5. Only the sensors on the upper face were used in this study. In all cases, the accelerometers measure the acceleration in the direction of the local normal of the structure. As in the previous configurations, different add-on masses were screwed onto the structure between nodes 2 and 3, and node 5 and 6, respectively, to emulate damage.

Cracks were also analyzed in both the composite and the PVC beam, as shown in Fig. 6. The information of the cracks corresponds to damage cases m13 and m14 in Table 3.

4.1. Damage cases

As mentioned before, both added masses and cracks were studied as damage features. The damages in this work were simulated by placing different masses of 154 g, 124 g, and 104 g in the central part of the upper face of the structure. The mass positions and their positions are shown in Table 3. The table also includes the corresponding information about the damage cases where cracks have been applied to the test structure. One crack was studied in the case of the composite beam, whereas one and two cracks, respectively, were analyzed in the PVC tube. All in all, three different configurations and twelve different damage cases were analyzed in this work, providing a reasonable empirical data basis. Masses of different weights were used to assess a possible systematic evolution of the damage signal, given the convenience of modifying the damage intensity by adding and removing masses. Cracks were included for proof of concept.

5. Results

This section presents the results for the different damage cases analyzed in Table 3. The damage detection methodology used is the one previously explained in Section 3. Before discussing the damage detection cases some basic results of the modal identification process and the accuracy of the modal reconstruction will be reported.

5.1. Results for the composite beam in the cantilevered configuration

5.1.1. Modal frequencies

The modal frequencies obtained for the case of the composite thin-wall beam in the cantilevered configuration are shown in Table 4. The predominant effect of the attached mass can be seen in the first mode, where a reduction of the modal frequency of up to 18 % can be observed. Also, a trend towards smaller frequency as the mass increases can be

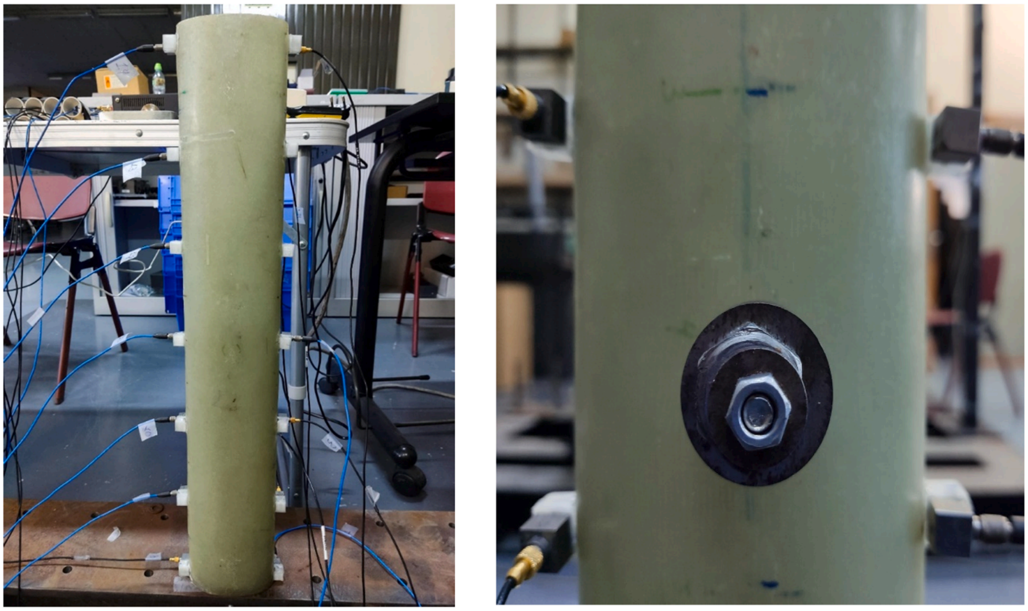

Fig. 3. *Left*: Test structure 1, a composite thin-walled beam (CTWB) with constant elliptical section, instrumented with two sets of seven uniaxial accelerometers each, being tested in a cantilever configuration. *Right*: Added mass screwed to the structure using a nut and a bolt, intended to emulate damage.

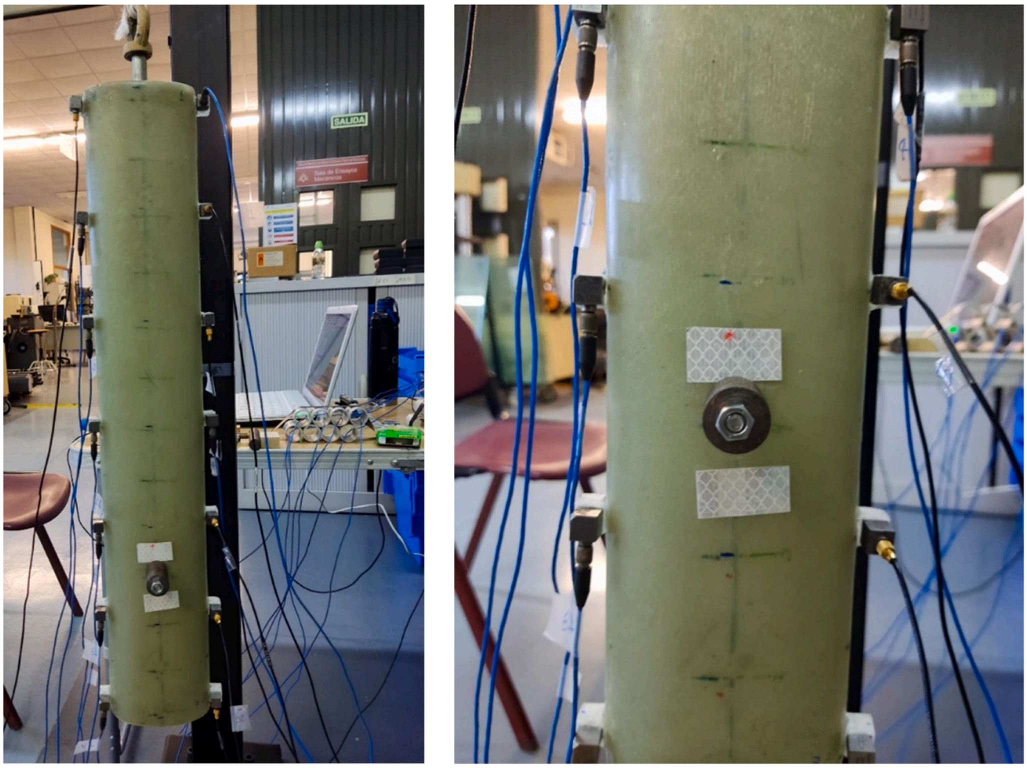

Fig. 4. *Left*: Test structure 1 (Composite thin-walled beam (CTWB)) tested in a suspended configuration. *Right*: Mass screwed onto the central part of the ellipse.

observed, with the mass of 154 g causing a frequency reduction of about twice the value observed for 74 g. This general reduction in frequency is consistent with the notion of a higher oscillating mass with roughly the same restitutive forces. Modes 2 to 4 show very small changes in response to the added mass, and no consistent progression can be observed with mass. Modes 5 and 6 show a small increase in frequency, but again no consistent progression with mass can be observed. Given that modal frequencies are generally relative insensitive to the presence of damage and generally do not provide any information on the location of the damage feature, modal frequencies will not be discussed any further in the remainder of this work.

5.1.2. Modal surfaces

Modal surfaces, both for the base case of now attached mass, and the case of the largest attached mass of 154 g, have been plotted in Fig. 7. Modes 1, 2, 5, and 6 can be seen to be largely symmetrical, whereas modes 3 and 4 are antisymmetric. The presence of the damage feature (attached mass) can be seen to affect mostly the higher modes, with the

Fig. 5. Suspended PV tube in a free-free configuration.

Fig. 6. Cracks analyzed in the two test structures. *Left*: Composite ellipse. *Right*: PVC tube.

Table 3
Damage cases analyzed.

Damage case	mass [g] or crack	location
Elliptical CTWB cylinder in cantilever configuration		
m1	154	5.4
m2	124	5.4
m3	104	5.4
Suspended elliptical CTWB cylinder with free end		
m5	154	5.4
m6	124	5.4
m7	104	5.4
m9	1 crack	~5
PVC tube in free-free configuration		
m10	154	5.5
m11	154	2.5
m12 (2 masses)	154	2.5 & 5.5
m13	1 crack	3
m14	2 cracks	3 & 5

Table 4
Modal frequencies for different mass cases: cantilevered composite TWB.

Mode	$m = 0$ g	$m = 74$ g	$m = 104$ g	$m = 124$ g	$m = 154$ g
1	26.86	24.41	24.41	21.97	21.97
2	480.96	490.72	490.72	488.28	488.28
3	749.51	754.40	754.40	754.39	749.51
4	1035.16	1025.39	1020.51	1027.83	1003.42
5	1181.64	1242.68	1240.23	1235.35	1232.91
6	1870.12	1943.36	1955.57	1953.13	1943.36

largest effects occurring at modes 4 and 6.

5.1.3. Accuracy of mode shape reconstruction

In order to assess the accuracy of the mode shape reconstruction two similarity concepts have been applied: (1) Self-similarity between independent instances of mode reconstruction for a same given sample, (2) cross-similarity between mode shapes obtained from different samples. Both similarity concepts have been evaluated by two metrics, the Modal Assurance Criterion (MAC) [28], and the Fréchet distance [29]. The MAC metric for two mode shape vectors φ_r and φ_s is defined as follows:

$$\mathrm{MAC}(\varphi_r, \varphi_s) = \frac{\varphi_r^T \varphi_s}{\left(\varphi_r^T \varphi_r\right)\left(\varphi_s^T \varphi_s\right)} \tag{32}$$

where “T” stands for the transpose of either of the mode shape vectors. By construction, $0 \leq \mathrm{MAC} \leq 1$, with $\mathrm{MAC} = 1$ corresponding to a perfect match between the two mode shapes. The second metric used is the Fréchet distance $\mathrm{FD}(\varphi_r,\varphi_s)$ between two curves [29]. FD also varies between 0 and 1 ($0 \leq \mathrm{FD} \leq 1$), but – contrary to the MAC metric and as implied by the name – perfect similarity corresponds to $\mathrm{FD} = 0$. The Fréchet distance is an algorithmically determined metric which cannot be written in closed form. The MATLAB implementation by Tristan Ursell [30] has been used in this work. In all cases, the predominant mode shapes defined in Eq. (23) have been used.

Fig. 8 shows the results of this similarity assessment for the case of the cantilevered CTWB structure. In the case of measurement pairs consisting of two independent measurements of the mode shapes (each corresponding to a stream of measurements of the same sample taken during 5 min as described in Section 4), referred to in Fig. 8 as “self-similarity”, it can be seen that MAC values for these cases are very close to 1 for all modes (1 to 6). Correspondingly, the Fréchet distances are very close to 0 in all self-similarity cases. As far as “cross-similarity” is concerned, i.e., the similarity between the mode shapes determined for two different samples, it can be seen that the MAC value is still close to 1 for the first three modes, but significantly smaller for the higher modes. The Fréchet distance, on the other hand, can be seen to be a much more sensitive metric, as a marked difference between the self-similarity and the cross-similarity cases arises even at the lower modes. In either case, two clear conclusions can be drawn from Fig. 8: (a) Different instances of mode determination for a same sample yield consistent results, (b) mode shapes belonging to different samples can be clearly distinguished.

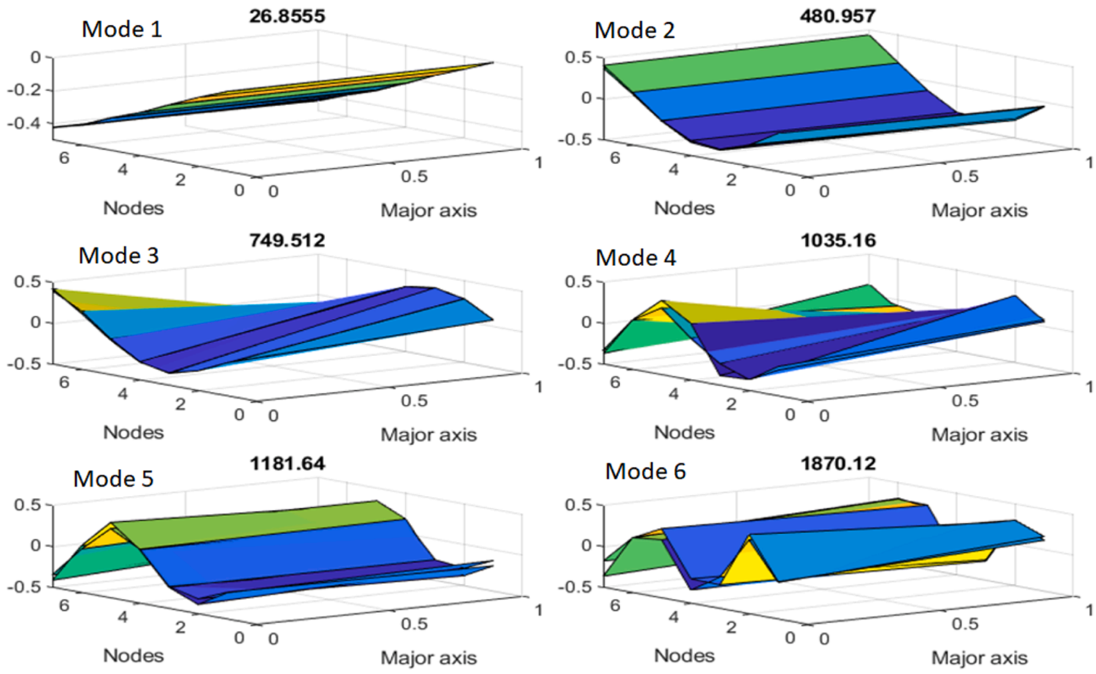

Fig. 7. Modal surfaces for the first six modes of the cantilevered composite TWB. Both the case of no added mass and the case with an attached mass of 154 g have been shown. Frequency values correspond to the case without added mass and are given in Hz.

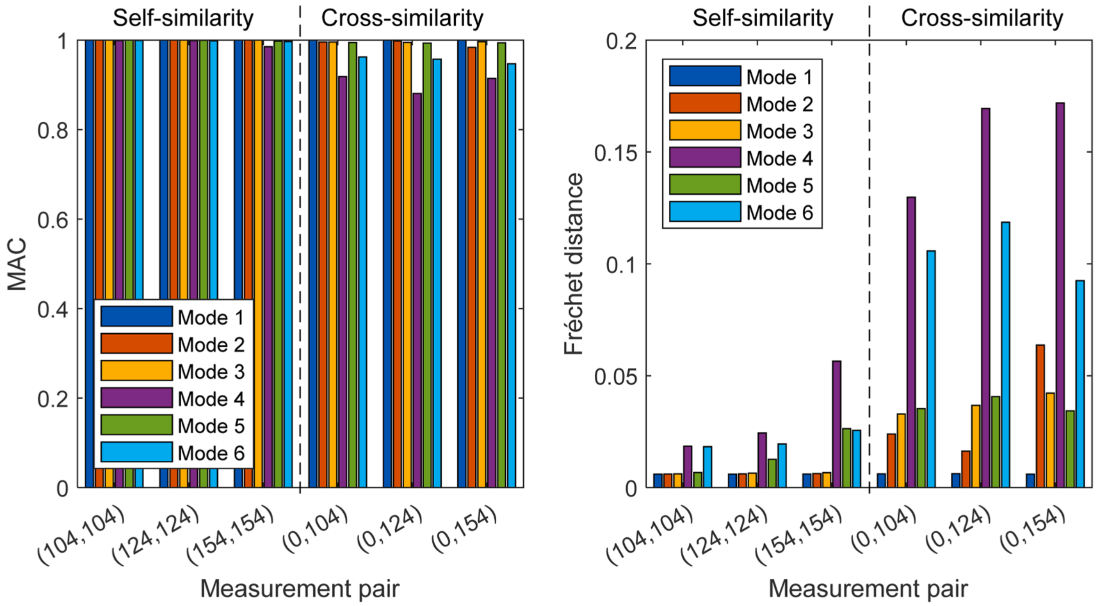

Fig. 8. Self- and cross-similarity of mode shapes of corresponding orders determined experimentally for the case of the cantilevered composite thin-wall beam with attached weights of 0 g, 104 g, 124 g, and 154 g. *Left*: Similarity as determined by the Modal Assurance Criterion (MAC). *Right*: Fréchet distance between mode shapes. Nomenclature: (m_i, m_j) = pair formed by samples with attached weights m_i and m_j (in g), respectively.

5.2. *Damage detection results for composite beam with elliptical cross section: cantilever configuration*

Fig. 9 shows the mode shapes as acquired with the two sets of seven sensors on either side of the beam as shown in Fig. 3. Two types of mode shapes can be readily distinguished: (1) Beam or deflectional modes, i.e., modes where both sides move in unison and (2) torsional modes where the two sides oscillate with similar amplitudes but with opposite sign. Modes 1, 2, 5, and 6 can be seen to have a predominantly deflectional character, whereas modes 3 and 4 are mostly torsional.

In Fig. 10 the predominant components of modes shapes have been shown, both for the case without damage, as well as with an attached weight of 154 g. As mentioned before, the predominant components for modes 1, 2, 5, and 6 correspond to the symmetric and modes 3 and 4 to the asymmetric combinations, as can be easily verified through the inspection of Fig. 9. It is interesting to observe that the shape of the symmetric component for mode 2 and the asymmetric component for mode 3 are very similar. A similar situation arises for the predominant components of mode 4 (antisymmetric) and 5 (symmetric).

The comparison between the predominant components of the healthy and the damaged structure demonstrates that the attachment of a mass of 154 g does not substantially alter the shapes of modes 1, 2, 3,

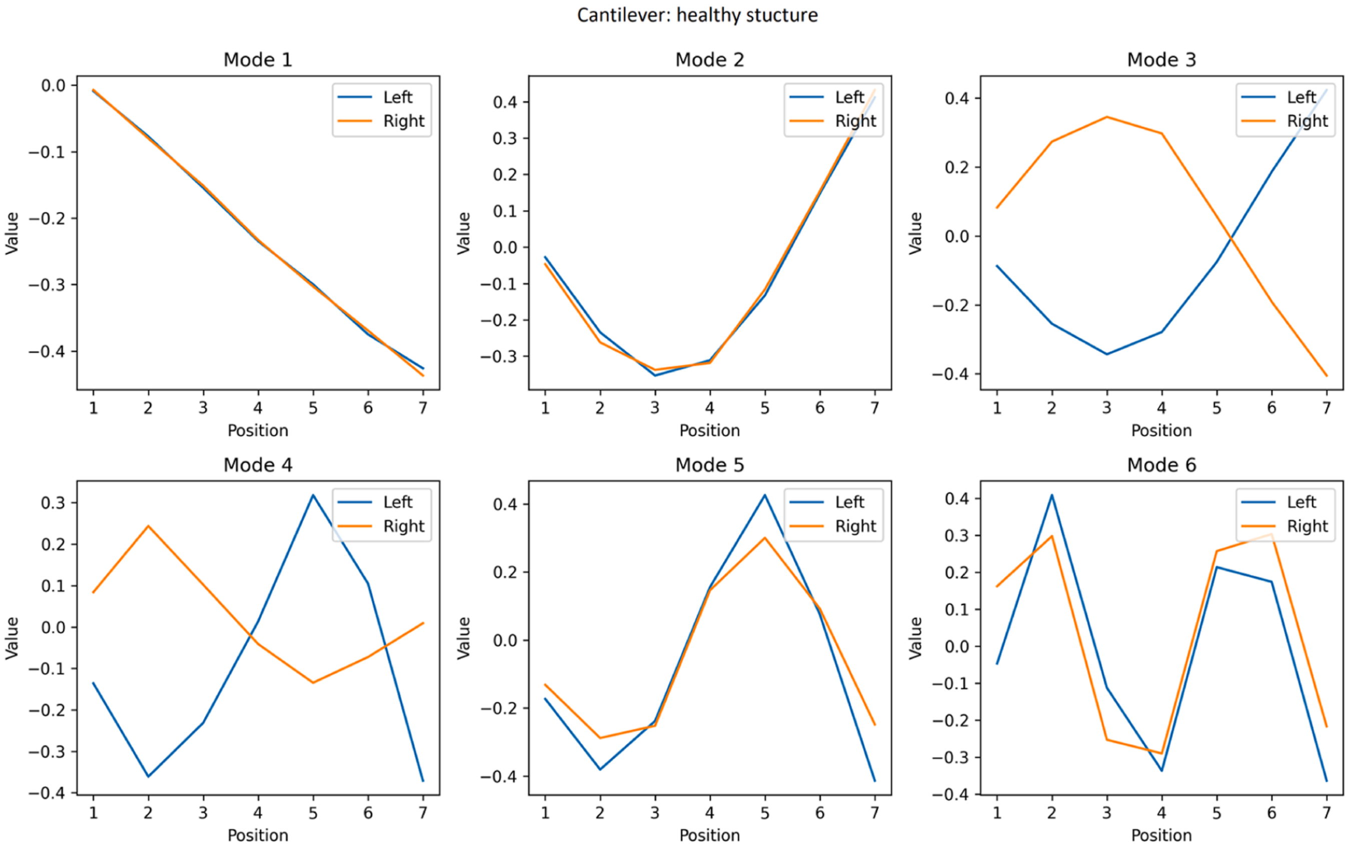

Fig. 9. OMA-determined mode shapes for the mode shapes of the undamaged ("healthy") TWB structure in cantilever configuration, i.e., with no attached weight. Accelerometers are located at integer values of the position coordinate. All mode shapes were obtained directly with the SSI method described in Section 2, with no additional processing.

and 5, but does have a significant effect on mode shape 4 and, to a lesser degree, on mode shape 6. The fundamental mode (number 1) is evidently very insensitive to damage features in general due to the lack of structure of this mode shape in general. The absence of a damage signal at modes 2 and 3, on the other hand, can be readily explained by the fact that the damage feature, i.e., the attached mass of 154 g, is attached near position $v = 5.4$, where modes 2 and 3 have a very small amplitude.

Higher modes should be generally more sensitive to localized damage features, which is indeed what is observed, since modes 4 and 6 (though not 5) show a clear modification of the (predominant component of the) mode shape near the damage location. Ideally, torsional modes like mode 4 should have low sensitivity to centrally mounted damage features, but a number of asymmetries are easily introduced into the experimental arrangement, including the mounting of the mass and the corresponding displacement and possible tilting of the principal axis of the beam. No clear rationale for the absence of a damage signal at mode 5 has been identified though.

The benefit of using a specially designed damage metric over a mere visual inspection of the mode shapes can be appreciated in Fig. 11, where a progression of scalograms, i.e., 2D-plots of the damage metric $m_1(v,s)$, has been plotted for linear positions x along the beam axis, with integer values of v corresponding to the axial positions of the accelerometers, and the scale factor s ranging from 1 to 23. The damage feature near the mass position ($v = 5.4$) can be clearly distinguished. Moreover, there appears to be a monotonic increase of the damage signal with the value of the attached mass, as can be appreciated by a quick inspection of the color scales in each of the subplots. It is also conspicuous that side lobes of intensity (as seen around $v = 3$ and at the borders) are much smaller than the main signal, making it easy to discriminate the signal region by a simple threshold filter. A more complex discrimination scheme, based on the combination of two damage metrics, has been described and demonstrated by [8] and could be used if necessary.

It is worth noting that the damage feature appears quite neatly localized in the scalograms, with little signal corresponding to large (small s) and small (large s) structural features, but with a compact signal at intermediate values of the scale factor. This illustrates the usefulness of the wavelet transform approach, which is capable of sampling a signal at different spatial scales. The compact form of the signal in the (v, s)-plane prompted us to attempt a quantification of the damage signal through a bivariate Gaussian fit, as described in Section 3.5. As shown in Fig. 12, this approach works very well, with the bidimensional fit surfaces closely emulating the experimental damage signal.

Using the parameters obtained from the bivariate Gaussian fit a calibration curve can be constructed. Three metrics were used in this case: (1) The area under the bivariate Gaussian fit surface, (2) the area under the experimental data surface $m_1(v,s)$, clipped to the zone of interest, and (3) the peak value of the Gaussian fit surface. The results are shown in Fig. 13. The following observations can be made: (a) The damage signal increases approximately linearly with added mass in all cases, (b) the direct use of the area under the experimental data surface $m_1(v,s)$ and the Gaussian fit yield very similar results, (c) the use of the peak of the Gaussian fit surface provides a better linearity and therefore a better calibration curve, (d) there is a threshold value for damage detection, i.e., a minimum value of the added mass is required to cause a reliable signal. If the maximum value of the bivariate Gaussian fit surface is taken as the damage metric, then this threshold value is ~ 95 g, i. e., added masses below that value cannot be detected reliably.

The final comment in this section concerns the accuracy and the precision of the method in the localization of the damage feature, i.e., the attached mass. The accuracy of the measurement, i.e., the ability to

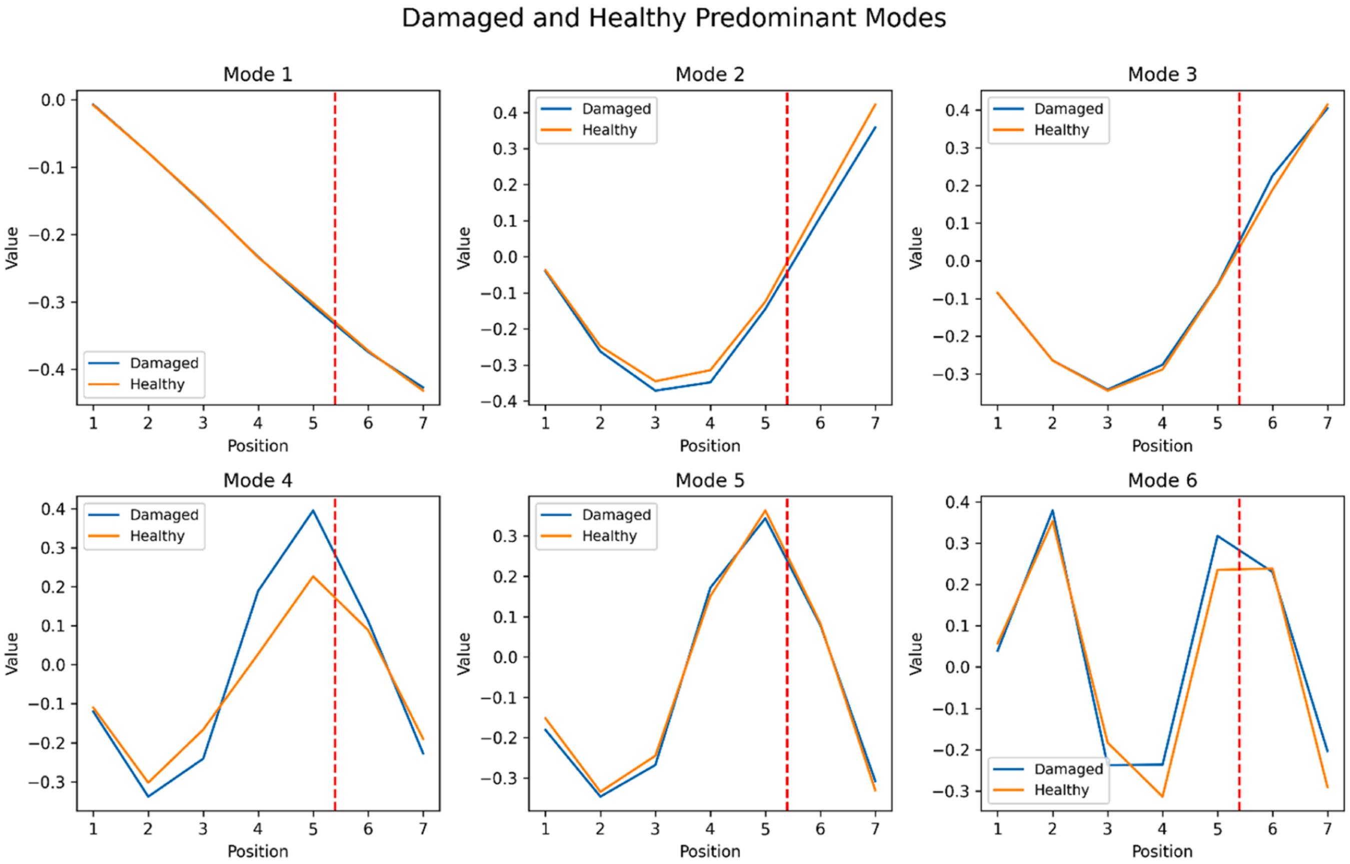

Fig. 10. OMA-determined *predominant* components for the mode shapes of the TWB structure in cantilever configuration with no attached weight ("healthy structure") and with an attached weight of 154 g. Predominant components were calculated according to the procedure in Section 3.2. The dotted line indicates the location of the added mass.

detect the true position of the added mass can be assessed as the bias between the true position and center of the Gaussian fit surface. Precision, on the other hand, is the uncertainty associated with the determination of the center position of the Gaussian fit surface. Fig. 14 provides the corresponding information, by showing sections of both the experimental surface $m_1(v,s)$ and the Gaussian fit surface at the location s_0 where the Gaussian surface has its maximum. It can be seen that the Gaussian curve provides a very good fit to the experimental data in the region of the damage feature for all three mass values; the small side lobes of the experimental signal can be seen to be negligible. The width of the Gaussian fit curve, as measured by twice the standard deviation can be seen to be around 0.8 (in units of the sensor separation), i.e., of the order of the cell size of the measurement grid, which is plausible. Also shown in Fig. 14 is the bias of the predicted position of the added mass, which can be seen to be slightly negative with absolute values between $\Delta v = 0.17$ and 0.23, equivalent to an accuracy range of 2.8 % to 3.8 % of the beam length. It is worth noting that this accuracy is well below the size of a grid cell, i.e., the distance between two adjacent sensor positions. This is no contradiction, but simply a consequence of the well-known fact that the average value of a series of measurements has a (much) smaller error than each individual measurement value.

5.3. Composite beam: suspended configuration – damage cases m5, m6, and m7

Since beams in practical applications may be subject to different boundary conditions it is interesting to investigate how the damage detection method presented in this work works in the second case, the one where the CWTB was suspended from the ceiling. It is instructive to inspect the modal structure of the healthy beam, i.e., without added masses. This is shown in Fig. 15. From the comparison with Fig. 9 it can be seen that significant changes in the modal structure occur upon changing the boundary conditions. The first mode reflects the increased mobility of the beam at the suspension point, although the motion can still be seen somewhat restricted. This restriction becomes irrelevant at higher modes, with can be seen to behave almost like the modes of a beam with two free ends. Mode 1 is symmetric, i.e., corresponds to a flexional motion, as well as mode 2. The almost free behavior of the suspended end in the higher flexional modes (2 and 6) can be readily interpreted in terms of the fact that the beam motion is approximately perpendicular to the suspending chord, as long as the motion is limited to small amplitudes. To the extent the motion increases in size a force of restitution appears because of gravity, since the suspension is forced to move along an arc segment. Modes 3, 4, and 5 are now torsional, which is a departure from the cantilever case, where only modes 3 and 4 were torsional. Modes 3 and 4 show a slight asymmetry, which mode 4 showing some admixture from the symmetric component. Mode 6 is again symmetric or flexional, as in the cantilever case.

The effect of an added mass of 154 g on the modal structure of the suspended beam can be seen in Fig. 16. For the sake of brevity, only the predominant components are discussed. It can be seen that, similarly to the case of the cantilever, the strongest damage signal comes from the fourth mode, where a clear modification of the mode shape in the vicinity of the added mass can be observed. As opposed to the cantilever case, no effect of the mass on the other mode shapes can be observed.

As in the case of the cantilever configuration, an attempt was made to construct a calibration curve based on the damage signal constructed in three different ways, i.e., the area under the bivariate Gaussian fit surface, the area under the measured scalogram in the damage region, and the maximum value of the Gaussian fit surface. The results are shown in

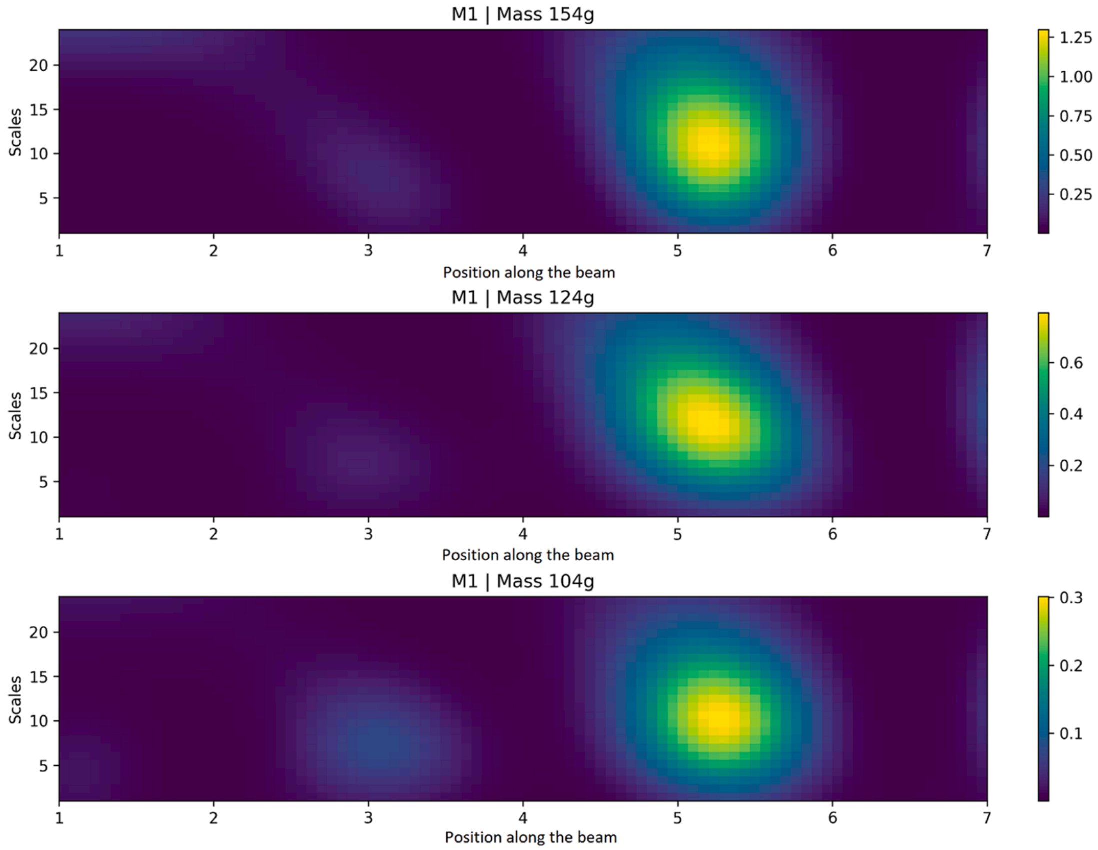

Fig. 11. Scalogram for the damage metric as a function of the attached weight for the case of the cantilever configuration. Accelerometers along the beam are located at integer values of the position coordinate. Scalogram values for positions with non-integer values were obtained through interpolation.

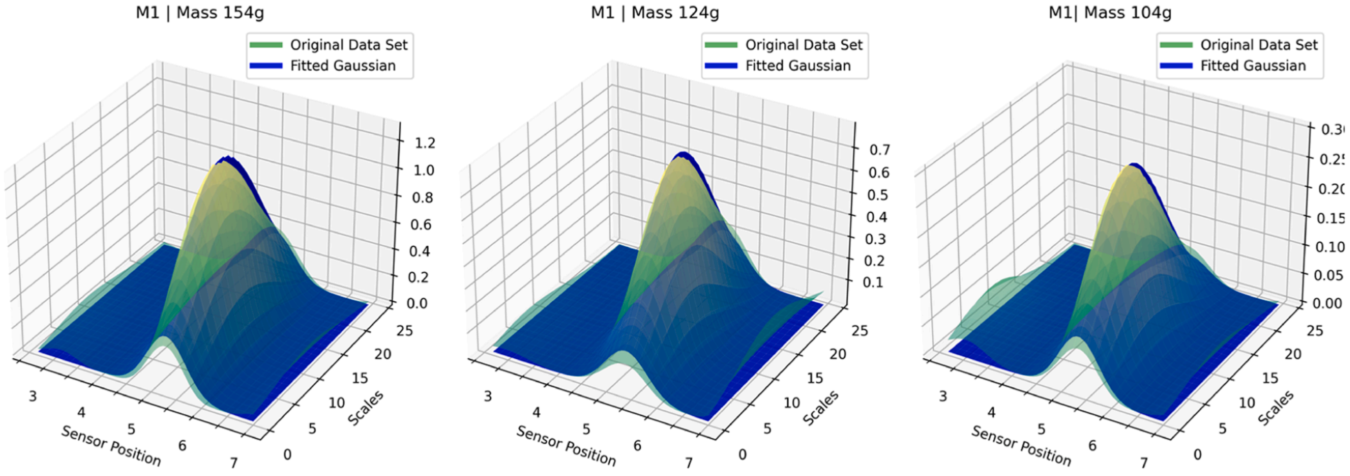

Fig. 12. Three-dimensional representations and bivariate Gaussian fits to the damage scalograms $m_1(v,s)$ as a function of the sensor position v and the wavelet scale s for the three damage cases $m = 104$ g, 124 g, and 154 g and the cantilever configuration.

Fig. 17. The results can be seen to be very similar to the cantilever case, with the maximum values of the bivariate Gaussian fit surface again providing the most linear evolution as a function of the added mass. This damage metric therefore appears to be the most appropriate one for damage quantification purposes. It should be noted, however, that – as in the case of the cantilever configuration – the linear calibration curve does not go through the origin, i.e., shows a threshold behavior. If again the maximum value of the bivariate Gaussian fit surface is taken as the damage metric, then this threshold value is ~ 95 g, in consistency with the cantilever case. This was verified by placing smaller added masses on the beam; while it was possible to occasionally obtain a damage signal, the results did not prove to be consistent, in agreement with the conclusion that a threshold value for reliable damage detection of about 95 g exists in this experimental configuration.

5.4. Suspended CTWB structure with one crack – damage case m9

After studying the effect of simulated damage through the addition of masses to the beam surface the effect of an actual damage feature was analyzed as well. The scalogram for this case can be seen in Fig. 18. A

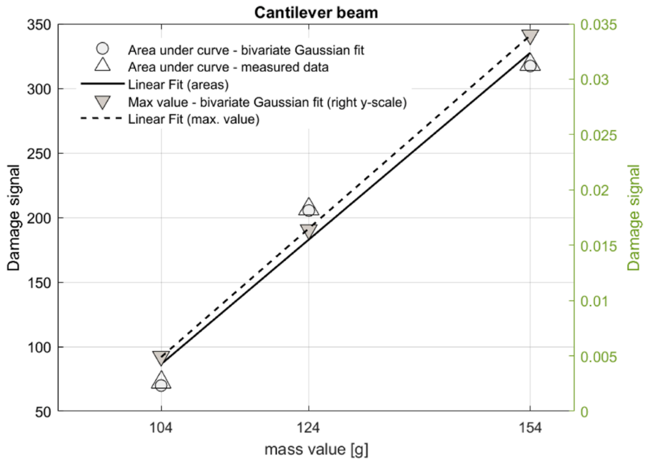

Fig. 13. Calibration curve for the damage signal for the composite thin-wall beam (CTWB) in the cantilever configuration.

clear damage feature is conspicuous at the vicinity of the position of sensor 5, which coincides with the actual position of the crack. Some side lobe intensity is near position $x \sim 3$ and particularly at scale factors in the range of $s \sim 3\ldots5$ can be appreciated as well. Such side lobes may occur as the result of the wavelet transformation. Discrimination of the true signal can be achieved through the application of a threshold filter or more sophisticated metrics such as described in [9].

5.5. Free-free PVC tube with added masses – damage cases m10, m11, and m12

In order to demonstrate the methodology proposed in this work with another type of sample, a PVC tube was analyzed in a free-free configuration, as described in Section 4 and shown in Fig. 5. As summarized in Table 3, three damage combinations were applied to the tube: (a) an added mass in the left part of the tube, (b) an added mass in the right part, and (c) two simultaneous masses in the left and right part, respectively. The results are shown in Fig. 19, where the damage scalograms for the three cases mentioned have been displayed jointly. As in the case of the CTWB structure, the added masses cause a very clear signal in the $m_1(v,s)$ scalogram, which closely relates with the position of the added masses. It is also conspicuous that two damage features can also be detected simultaneously, without an apparent overlap from the signals of each feature. It can also be noted that in this case the damage signal is located at smaller values of the scale factor, with most of the signal intensity being concentrated in the region of $s \sim 1\ldots3$, as opposed to the CTWB case, where the highest intensity was located around $s \sim 10$.

5.6. Free-free PVC tube with one and two cracks – damage cases m13 and m14

Our final test case concerns damage cases m13 and m14, where the PVC tube in its free-free configuration was tested for cracks. As in the case of the damage cases m10-m11, where massed had been added to simulate damage, in the case of actual damage features (cracks), clear damage signals appear in the $m_1(v,s)$ scalogram, both in the case of an individual crack (upper graph) and the case of two simultaneous cracks (see Fig. 20). The side lobe intensity, caused by the wavelet transform, is

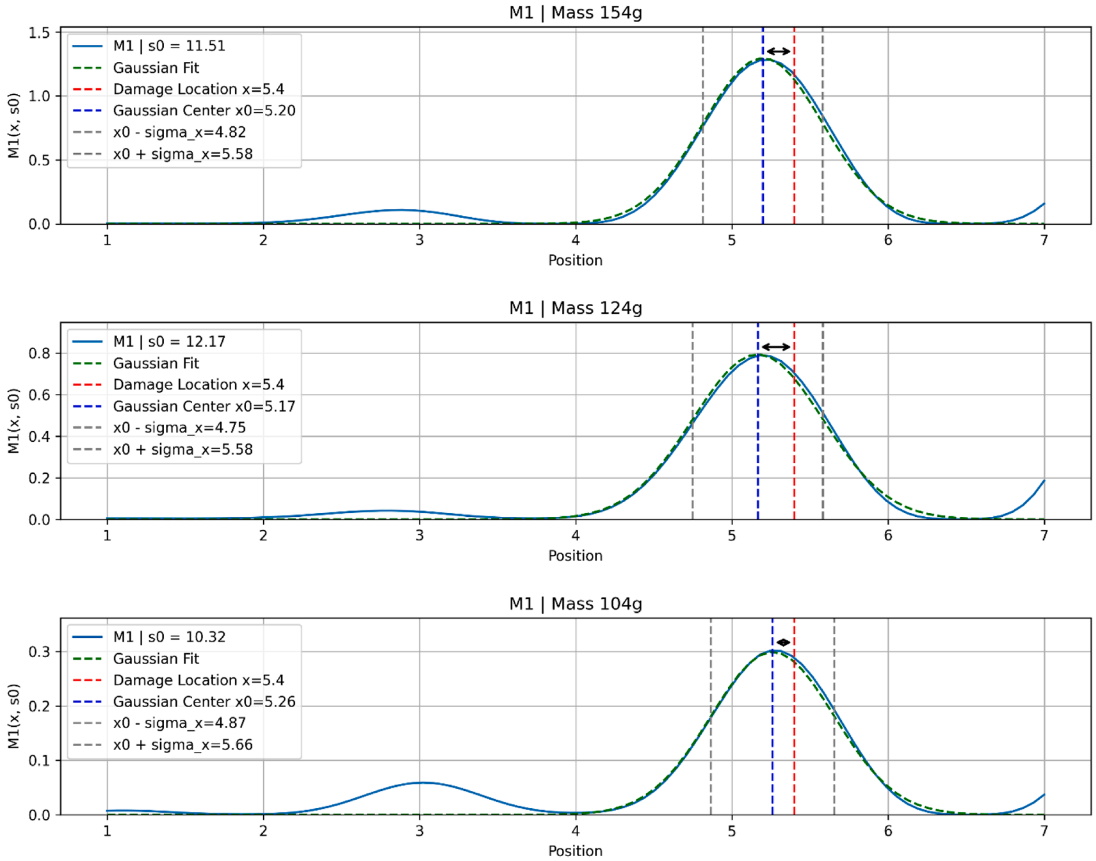

Fig. 14. Accuracy and precision of the localization of the damage feature (added mass) for the case of the cantilevered composite beam. The continuous lines show the section $m_1(v,s_0)$, with v being the axial coordinate and s_0 the scale factor value where m_1 has its maximum; the Gaussian fit is shown as a dotted line.

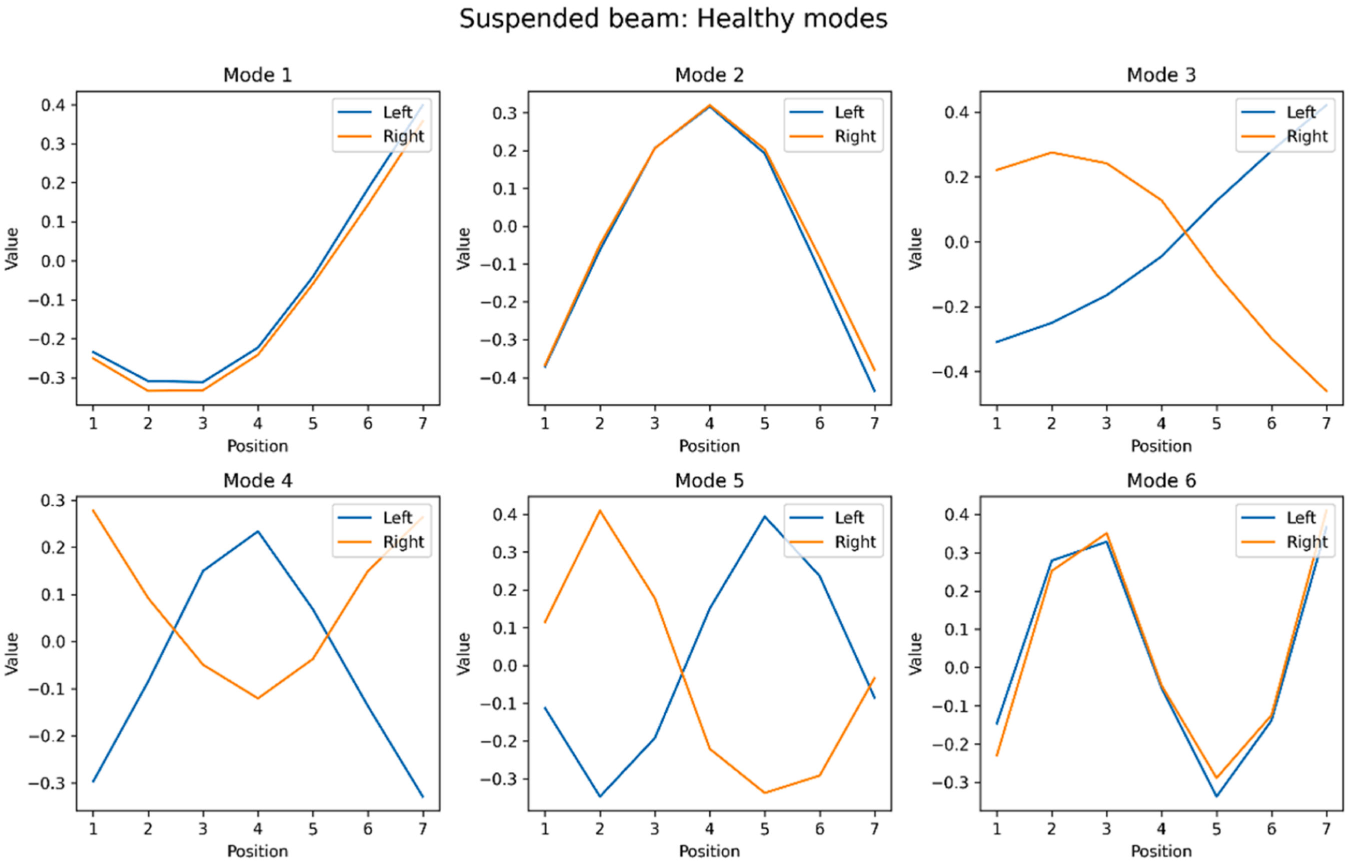

Fig. 15. OMA-determined mode shapes for the mode shapes of the undamaged ("healthy") TWB structure, i.e., with no attached weight, in the suspended configuration. Accelerometers are located at integer values of the position. All mode shapes were obtained directly with the SSI method described in Section 2, with no additional processing.

somewhat higher than in the previous case; however, the signal levels at the true damage positions are significantly higher than at these side lobes, allowing for a reliable discrimination of the true signal from the background by simple automated procedures. As in the previous case, most of the signal intensity is concentrated at lower values of the scale factors.

6. Summary and conclusions

In the present work, the use of Operational Modal Analysis (OMA) for the detection of damage features has been studied on a variety of samples, measurement configurations, and damage features. The OMA-based methodology introduced in this work combines modal reconstruction using Stochastic Subspace Identification (SSI) and Continuous Wavelet Transform (CWT) with an interpolation and surface fitting approach of CWT-created damage maps built in (v, s)-space, with v being the axial coordinate and s the scale factor of the CW transform. The fitting process allows for both an accurate localization of the damage feature with sub-grid resolution, i.e., the ability to accurately locate damage between accelerometer locations, and for a quantification of the damage. In order to cover a range of damage features and samples, a composite thin-wall beam (CTWB) structure with elliptical cross section has been measured in both a cantilevered and a suspended configuration, with damage features including (a) a set of different additional weights attached to the structure, (b) one crack feature perpendicular to the beam axis, (c) two simultaneous cracks. Additionally, a PVC tube with circular cross section has been analyzed for both individual and twin cracks. In all cases the damage features could be located accurately. The case of the attached masses was designed to allow for a convenient variation of the intensity of damage; attached masses varied between 9.5 % and 14 % of the unloaded beam mass. In these cases, a linear variation with a threshold between the extra mass and the damage signal was found. The threshold value was found to be about 95 g, or 8 % of the mass of the CTWB structure. Cracks with a length of about 4 % of the perimeter could be detected in an individual and a twin configuration for both the CTWB and the PVC structure.

In the opinion of the authors, this work contributes to the state of the art of the field in several ways: (a) It provides a systematic assessment of a variety of samples, configurations, and damage features, as opposed to proof-of-concepts works which dominate most of the published work on OMA-based damage assessment in beams and plates. (b) It demonstrates that damage intensity can be quantified, and that to a good approximation a linear relationship exists between the damage signal and the damage intensity above a certain threshold. (c) It shows that accurate damage localization can be achieved with a relatively coarse measurement grid thanks to the interpolation and surface fitting approach put forward in this work. Seven pairs of accelerometers, distributed along the beam axis on symmetrical locations, were used in the case of the CTWB structures; this places our work on the lower end of the required number of sensors compared to the published work in literature. This points to an opportunity for creating cost-effective solutions for continuous structural health monitoring (SHM) of beam-like structures. It should be mentioned, though, that this advantage is relevant only for measurement systems based on discrete sensors (typically accelerometers), where a higher number of measurement locations translates into a higher cost. In the case of scanning methods, such as scanning laser vibrometer (SLV) techniques, a higher number of measurement locations, if within the capabilities of the instrument, does not mean a higher cost, making a direct comparison more difficult. It is worth noting, however, that SLV studies of damage in beams or plates have been

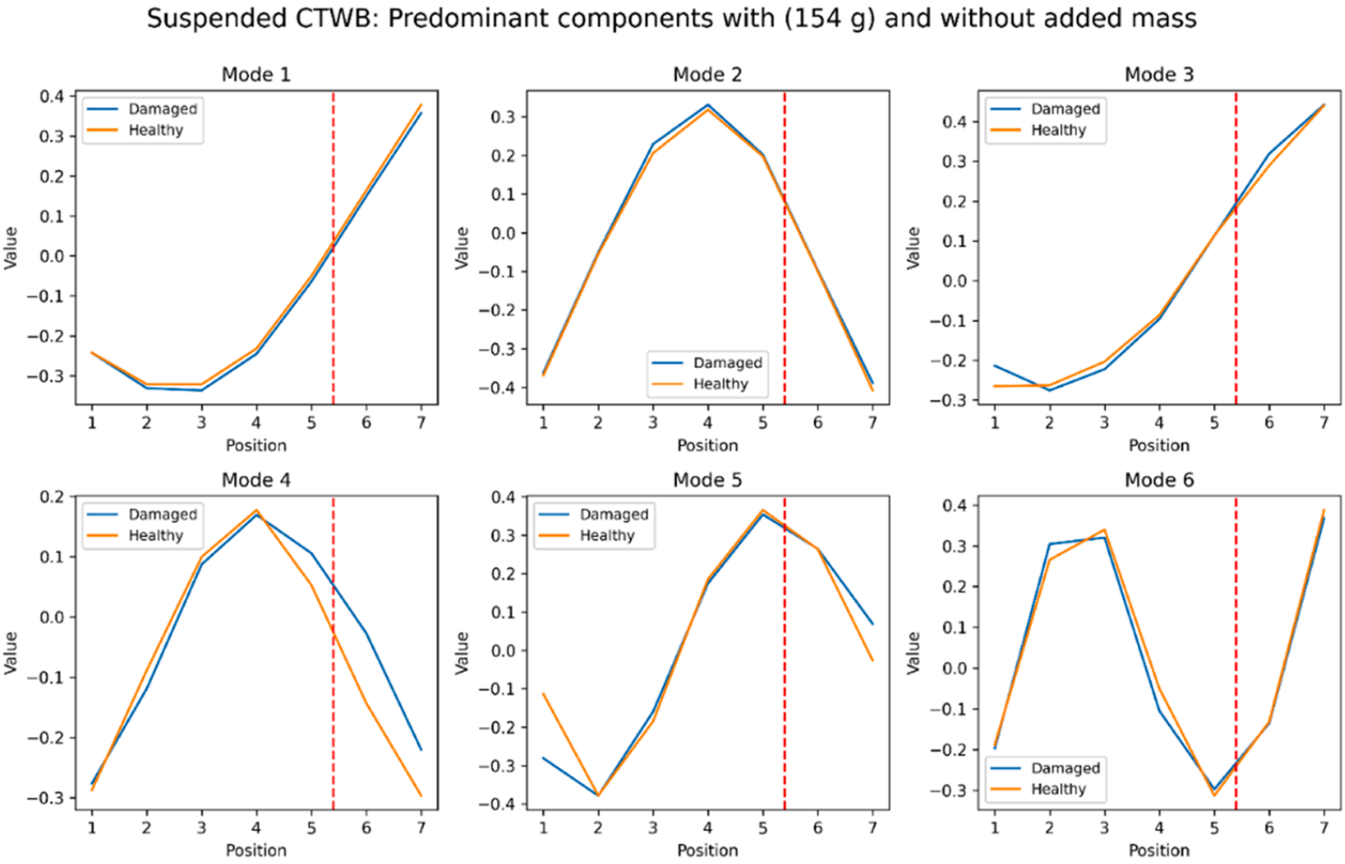

Fig. 16. OMA-determined *predominant* components for the mode shapes of the TWB structure in the suspended configuration with no attached weight ("healthy structure") and with an attached weight of 154 g. Predominant components were calculated according to the procedure in Section 3.2. The dotted line indicates the location of the added mass.

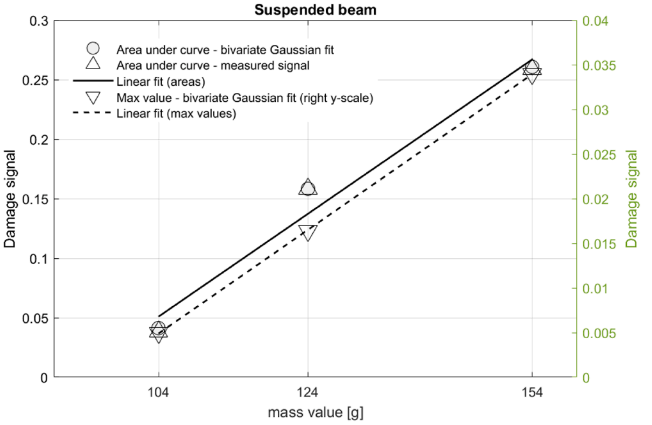

Fig. 17. Calibration curve for the damage signal for the composite thin-wall beam (CTWB) in the suspended configuration.

demonstrated mostly on simple structures; to the best knowledge of the authors, no SLV studies on damage detection, localization, and quantification have been conducted on composite thin-walled beams so far. (d) A final remark refers to the data processing requirements of the method proposed in this work: In times where much of the engineering research gravitates towards black box approaches with large data processing requirements, often based on machine learning techniques, it is important to demonstrate that lean methods, with low data processing requirements, may still be competitive solutions. Apart from being computationally cheaper, such methods also have the benefit of greater traceability and interpretability. We believe our work falls into this category.

Regarding future research necessities, there are several lines of work that should be pursued in the near future. Firstly, the threshold behavior for reliable damage detection and quantification should be analyzed in more detail, and methods to lower or avoid this threshold should be investigated. As shown by Pacheco et al. [8], measurement noise is a significant source of uncertainty in the mode shape reconstruction process. In the current study, no special measures were taken to address, quantify, or reduce noise from the measurement process; however, as shown by Pacheco et al. [8], the effect of noise can be drastically reduced with appropriate data processing schemes. Secondly, instrumentation that can be embedded into the sample should be investigated for a possible use in routine monitoring of critical engineering structures. A possible alternative is the use of fiber-optic sensors based on Bragg gratings (FBG sensors). Thirdly, the method presented in this work relies on the knowledge of the mode shapes of the undamaged structure, which may be viewed as a limitation. While baseline-free metrics for damage detection, such as the use of a suitable curvature index, have been studied in the past, including by the authors of this work, the availability of reliable information on the sample baseline generally allows for a much more robust detection scheme. The baseline problem can be solved in several ways, including the use of suitable digital twins [5] and the utilization of permanently installed instrumentation by embedding instruments into the structure, as mentioned above. This allows for a high-accuracy determination of the baseline mode shapes, given that the modes can be measured in a continuous way over extended periods of time, well before damage is expected to arise. Continuous monitoring can also detect incipient damage features in the very early stages, allowing for triggering of maintenance events. An

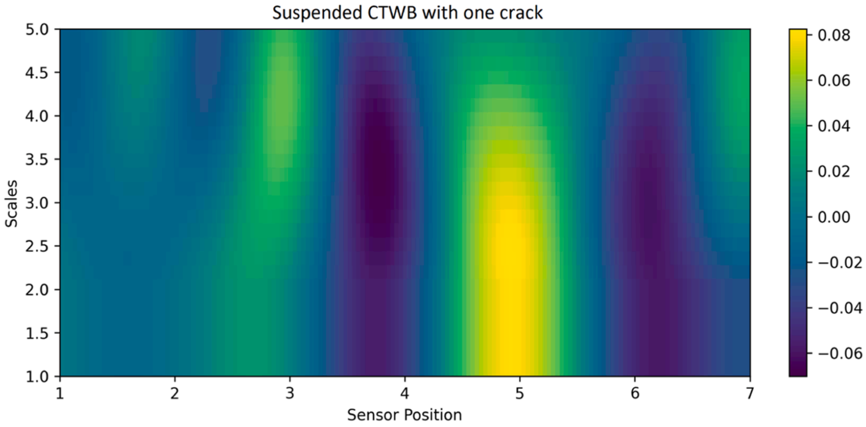

Fig. 18. Damage scalogram for the case of the suspended CTWB structure with one crack.

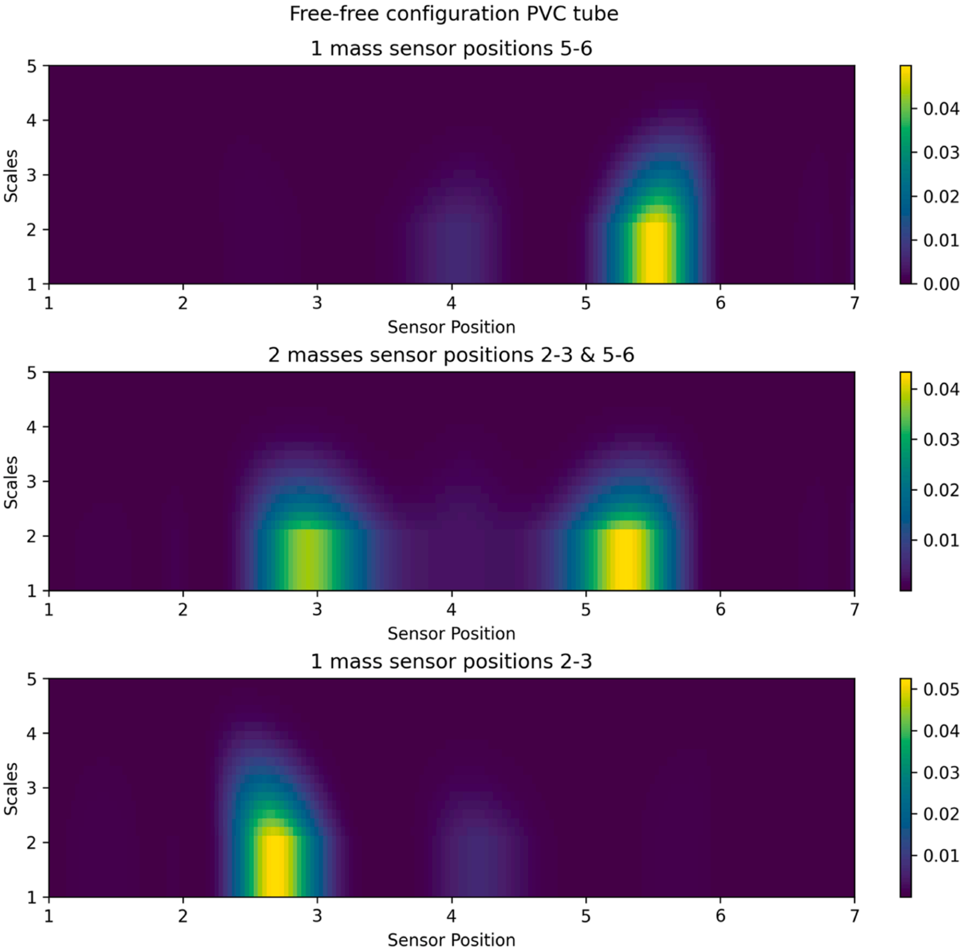

Fig. 19. Results obtained with the PVC tube in a free-free configuration. (Upper graph) One added mass between sensors 5 and 6. (Lower graph) One added mass between sensors 2 and 3. (Middle graph) Simultaneous presence of masses between sensors 2 and 3, and between 5 and 6.

obvious requirement for such a scheme to work is a high sensitivity to damage features; improving this sensitivity in realistic environments can therefore be expected to be an important line of work in the next years. The other requirement is the availability of low-cost solutions, in order to extend the benefits of Structural Health Monitoring (SHM) to machinery and infrastructure in general. An important example are offshore wind turbines, where high-stress conditions and high cost of maintenance events lead to challenging conditions for keeping the blades spinning over extended periods of time.

CRediT authorship contribution statement

Josué Pacheco-Chérrez: Writing – original draft, Visualization, Software, Investigation, Data curation. **Manuel Aenlle:** Supervision, Resources, Methodology, Conceptualization. **Pelayo Fernández:** Supervision, Methodology, Conceptualization. **Carlos Colchero:** Visualization, Software, Data curation. **Oliver Probst:** Writing – review & editing, Writing – original draft, Supervision, Methodology, Formal analysis, Data curation.

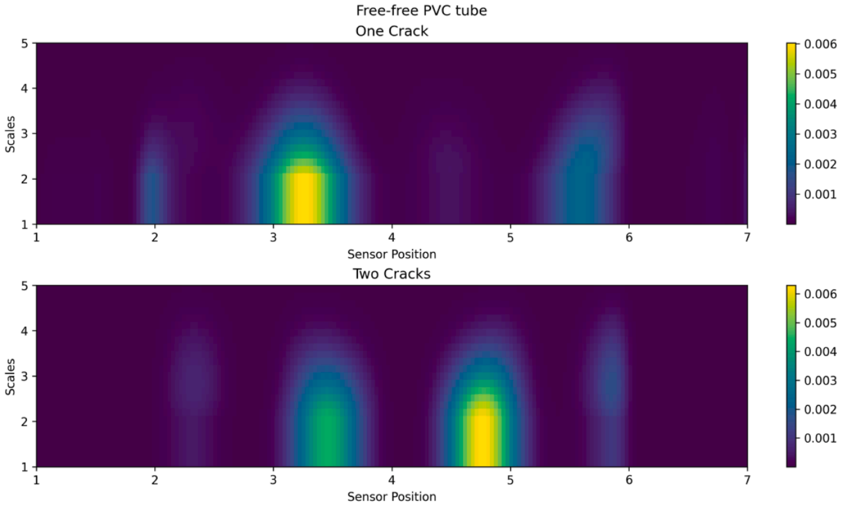

Fig. 20. Results obtained with the PVC tube in a free-free configuration, with one crack around $v = 3$ (upper graph) and two simultaneous cracks at around $v = 3$ and $v = 5$, respectively.

Declaration of competing interest

The authors declare that they have no known competing financial interests or personal relationships that could have appeared to influence the work reported in this paper.

Acknowledgments

J.P.C gratefully acknowledges a tuition waiver from Tecnológico de Monterrey for Ph.D. studies and a CONAHCYT stipend for living expenses. OP acknowledges support from the School of Engineering and Sciences at Tecnológico de Monterrey. M. Aenlle and P. Fernández appreciate support from the University of Oviedo.

Data Availability

Data will be made available on request.

References

[1] F.B. Zahid, Z.C. Ong, S.Y. Khoo, A review of operational modal analysis techniques for in-service modal identification, J. Braz. Soc. Mech. Sci. Eng. 42 (2020) 1–18, https://doi.org/10.1007/s40430-020-02470-8.

[2] K.F. Brethee, A.N. Uwayed, A.Y. Alden Qwam, A novel index for vibration-based damage detection technique in laminated composite plates under forced vibrations: experimental study, Struct. Heal. Monit. (2023), https://doi.org/10.1177/14759217221145622.

[3] M. Dahak, N. Touat, M. Kharoubi, Damage detection in beam through change in measured frequency and undamaged curvature mode shape, Inverse Probl. Sci. Eng. 27 (2019) 89–114, https://doi.org/10.1080/17415977.2018.1442834.

[4] Ł. Doliński, M. Krawczuk, A. Zak, Detection of delamination in laminate wind turbine blades using one-dimensional wavelet analysis of modal responses, Shock Vib. 2018 (2018), https://doi.org/10.1155/2018/4507879.

[5] J. Pacheco-Chérrez, A. Delgado-Gutiérrez, D. Cárdenas, O. Probst, Reliable damage localization in cantilever beams using an image similarity assessment method applied to wavelet-enhanced modal analysis, Mech. Syst. Signal. Process. 149 (2021), https://doi.org/10.1016/j.ymssp.2020.107335.

[6] J. Pacheco-Chérrez, D. Cárdenas, O. Probst, Experimental detection and measurement of crack-type damage features in composite thin-wall beams using modal analysis, Sensors 21 (2021) 8102, https://doi.org/10.3390/s21238102.

[7] S.S.B. Chinka, S.R. Putti, B.K. Adavi, Modal testing and evaluation of cracks on cantilever beam using mode shape curvatures and natural frequencies, Structures 32 (2021) 1386–1397, https://doi.org/10.1016/j.istruc.2021.03.049.

[8] J. Pacheco-Chérrez, A. Delgado-Gutiérrez, D. Cárdenas, O. Probst, Operational modal analysis for damage detection in a rotating wind turbine blade in the presence of measurement noise, Compos. Struct. 321 (2023) 1–12, https://doi.org/10.1016/j.compstruct.2023.117298.

[9] J. Pacheco-Chérrez, O. Probst, Vibration-based damage detection in a wind turbine blade through operational modal analysis under wind excitation, Mater. Today Proc. 56 (2022) 291–297, https://doi.org/10.1016/j.matpr.2022.01.159.

[10] E. Favarelli, A. Giorgetti, Machine learning for automatic processing of modal analysis in damage detection of bridges, IEEE Trans. Instrum. Meas. 70 (2021), https://doi.org/10.1109/TIM.2020.3038288.

[11] M. Xu, F.T.K. Au, S. Wang, H. Tian, Operational modal analysis under harmonic excitation using Ramanujan subspace projection and stochastic subspace identification, J. Sound. Vib. 545 (2023) 117436, https://doi.org/10.1016/j.jsv.2022.117436.

[12] W. Xu, W. Zhu, Y. Xu, M. Cao, A comparative study on structural damage detection using derivatives of laser-measured flexural and longitudinal vibration shapes, J. Nondestruct. Eval. 39 (2020) 1–17, https://doi.org/10.1007/s10921-020-00702-4.

[13] A.C. Altunışık, F.Y. Okur, S. Karaca, V. Kahya, Vibration-based damage detection in beam structures with multiple cracks: modal curvature vs. modal flexibility methods, Nondestruct. Test. Eval. 34 (2019) 33–53, https://doi.org/10.1080/10589759.2018.1518445.

[14] E. Di Lorenzo, S. Manzato, B. Peeters, V. Ruffini, P. Berring, P.U. Haselbach, et al., Modal analysis of wind turbine blades with different test setup configurations, Conf. Proc. Soc. Exp. Mech. Ser. 8 (2020) 143–152, https://doi.org/10.1007/978-3-030-12684-1_14.

[15] Y.F. Xu, D.M. Chen, W.D. Zhu, Operational modal analysis using lifted continuously scanning laser Doppler vibrometer measurements and its application to baseline-free structural damage identification, JVC/J. Vib. Control 25 (2019) 1341–1364, https://doi.org/10.1177/1077546318821154.

[16] J. Pacheco-Chérrez, O. Probst, Multiple damage detection in a cantilever beam using baseline-free operational modal analysis, Mater. Today Proc. J. 56 (2022) 433–439, https://doi.org/10.1016/j.matpr.2022.01.397.

[17] C. Rinaldi, J. Ciambella, V. Gattulli, Image-based operational modal analysis and damage detection validated in an instrumented small-scale steel frame structure, Mech. Syst. Signal. Process. 168 (2022) 108640, https://doi.org/10.1016/j.ymssp.2021.108640.

[18] A. Migot, V. Giurgiutiu, Numerical and experimental investigation of delamination severity estimation using local vibration techniques, J. Intell. Mater. Syst. Struct. (2022), https://doi.org/10.1177/1045389X221128585.

[19] A. Migot, H.N.H. Naser, A.A. Ugla, V. Giurgiutiu, Investigations of fatigue crack detection using local vibration techniques: numerical and experimental studies, J. Nondestruct. Eval. 42 (2023), https://doi.org/10.1007/s10921-023-00922-4.

[20] M. Abdulkareem, N. Bakhary, M. Vafaei, N.M. Noor, R.N. Mohamed, Application of two-dimensional wavelet transform to detect damage in steel plate structures, Meas J. Int. Meas. Confed. 146 (2019) 912–923, https://doi.org/10.1016/j.measurement.2019.07.027.

[21] Y. Xu, J.M.W. Brownjohn, D. Hester, Enhanced sparse component analysis for operational modal identification of real-life bridge structures, Mech. Syst. Signal. Process. 116 (2019) 585–605, https://doi.org/10.1016/j.ymssp.2018.07.026.

[22] W. Xu, W. Zhu, M. Cao, H. Wu, R. Zhu, A novel damage index for damage detection and localization of plate-type structures using twist derivatives of laser-measured mode shapes, J. Sound. Vib. 481 (2020) 115448, https://doi.org/10.1016/j.jsv.2020.115448.

[23] Structural Vibration Solutions. ARTeMIS Modal 2022.

[24] Andersen P. Technical paper on the stochastic subspace identification techniques 2010:1–14.

[25] R. Brincker, P. Andersen, Understanding stochastic subspace identification, in: Proceedings of the Conference Proceedings of the Society for Experimental Mechanics Series, 2006.

[26] B. Peeters, G De Roeck, Reference-based stochastic subspace identification for output-only modal analysis, Mech. Syst. Signal. Process. 13 (1999) 855–878, https://doi.org/10.1006/mssp.1999.1249.

[27] A. Messina, Refinements of damage detection methods based on wavelet analysis of dynamical shapes, Int. J. Solids. Struct. 45 (2008) 4068–4097, https://doi.org/10.1016/j.ijsolstr.2008.02.015.

[28] M. Pastor, M. Binda, T. Harčarik, Modal assurance criterion, Procedia Eng. 48 (2012) 543–548, https://doi.org/10.1016/j.proeng.2012.09.551.

[29] Fan C., Raichel B. Computing the Fréchet Gap Distance. vol. 65. Springer US; 2021. 10.1007/s00454-020-00224-w.

[30] Tristan U.. Frechet distance calculator. MATLAB Cent File Exch 2024. https://www.mathworks.com/matlabcentral/fileexchange/41956-frechet-distance-calculator (accessed October 21, 2024).